EISCAT

EUROPEAN INCOHERENT SCATTER SCIENTIFIC ASSOCIATION

ANNUAL REPORT 2021–2022

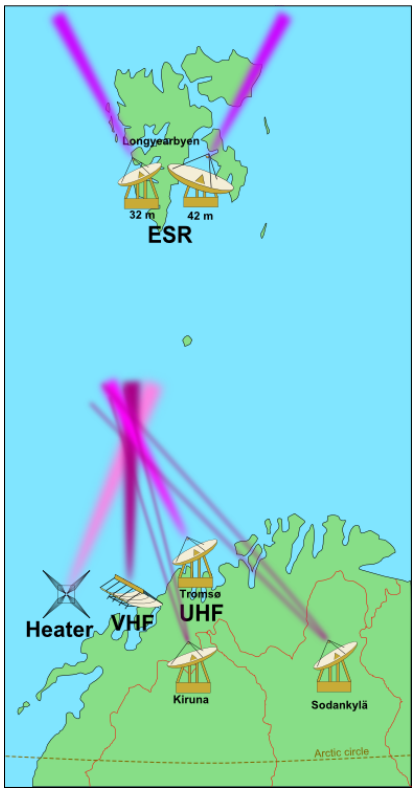

EISCAT Radar Systems

Location		Tromsø	Kiruna	Sodankylä	Longyearbyen	
Geographic coordinates		69°35′N 19°14′E	67°52′N 20°26′E	67°22′N 26°38′E	78°9′N 16°1′E	
Geomagnetic inclination		77°30′N	76°48′N	76°43′N	82°6′N	
Invariant latitude		66°12′N	64°27′N	63°34′N	75°18′N	
Band	UHF	VHF	VHF	VHF	UHF	
Frequency (MHz)	929	224	224	224	500	
Maximum bandwidth (MHz)	8	3	8	8	10	
Transmitter	2 klystrons	1 klystron	-	-	16 klystrons	
Channels	6	6	6	6	12	
Peak Power (MW)	2.0	1.6	-	-	1.0	
Average power (MW)	0.25	0.20	-	-	0.25	
Pulse duration (ms)	0.001–2.0	0.001–2.0	-	-	0.0005–2.0	
Phase coding	binary	binary	binary	binary	binary	
Minimum interpulse (ms)	1.0	1.0	-	-	0.1	
Digital processing	14 bit ADC on IF, 32 bit complex autocorrelation functions, parallel channels					
					Antenna 1	**Antenna 2**
Antenna	parabolic dish 32 m steerable	parabolic cylinder 120 m × 40 m steerable	parabolic dish 32 m steerable	parabolic dish 32 m steerable	parabolic dish 32 m steerable	parabolic dish 42 m fixed
Feed system	Cassegrain	line feed 128 crossed dipoles	crossed dipole	crossed dipole	Cassegrain	Cassegrain
System temperature (K)	90	250	100	100	80	65
Gain (dBi)	48.1	46	35.4	35.4	42.5	44.8
Polarisation	circular	circular	any	any	circular	circular

EISCAT Heating Facility (Tromsø)

Frequency range: 4.0 MHz to 8.0 MHz, Maximum transmitter power: 12×0.1 W, Antennas: Array 1 (5.5 MHz to 8.0 MHz) 30 dBi, Array 2 (4.0 MHz to 5.5 MHz) 24 dBi, Array 3 (5.5 MHz to 8.0 MHz) 24 dBi.
Additionally, a Dynasonde is operated at the heating facility.

Cover picture: Unloading of EISCAT_3D AU at Tromsø in September 2022 (Photo: Johan Svensson).

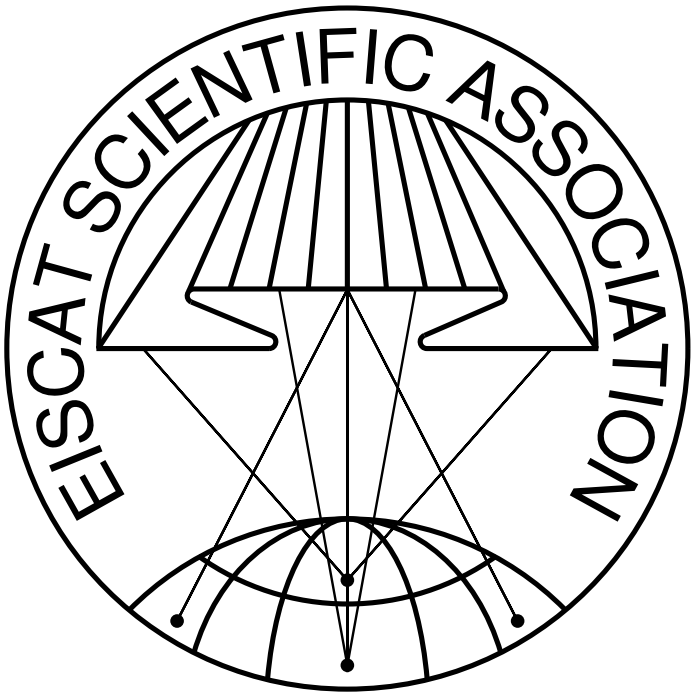

EISCAT Scientific Association
2021–2022

The EISCAT Scientific Association exists to provide scientists with access to incoherent scatter radar facilities of the highest technical standard

- *by developing and operating a continuing program of observatory measurements in cooperation with other ground-based and space-borne instruments and as part of the global network of incoherent scatter radars, the EISCAT Scientific Association seeks to provide a long-term database of ionospheric measurements of the highest quality.*
- *by supporting and operating the particular experiments of individual, and groups of, visiting scientists, EISCAT seeks to allow its users to address the widest possible range of research activities particularly in the areas of geospace and basic plasma physics.*
- *by providing leadership in the design and construction of hardware and software to support these goals, the EISCAT Scientific Association seeks to provide educational opportunities for young scientists and to foster appropriate Knowledge Transfer and Economic Impact.*
- *by developing and maintaining a well-founded science strategy, EISCAT seeks to provide a framework for the development of EISCAT-supported science and for the evaluation and development of scientific programs within the overall field.*

The scientific strategy of EISCAT is to understand the various forms of coupling between the Sun, the interplanetary medium, the terrestrial magnetosphere, ionosphere, and atmosphere of the high-latitude regions, natural and anthropogenic forcing, and related plasma physics and dynamics, and to achieve the necessary knowledge, understanding, principles, and techniques which would allow mankind to monitor, predict, and mitigate such processes within the next 30 years.

The specific goals of EISCAT are to develop large-scale facilities, techniques, and methods and, together with other ground-based and space-borne instruments, and as part of the global network of incoherent scatter and other middle and upper atmosphere radars, to encourage and undertake high quality research related to the global goal through studies addressing

- *behaviour and energy budget of the high-latitude regions, including space weather effects.*
- *fundamental plasma physics and dynamic processes in the near-Earth space environment.*
- *trends in atmospheric and ionospheric conditions, including long-term global change.*
- *properties and dynamics of the interplanetary environment.*
- *parametrisation of these processes and the development of techniques for their prediction.*

The investments and operational costs of EISCAT are shared between:

China Research Institute of Radiowave Propagation, People's Republic of China
National Institute of Polar Research, Japan
Norges forskningsråd, Norway
Suomen Akatemia, Finland
UK Research and Innovation, United Kingdom
Vetenskapsrådet, Sweden

Contents

Scientific highlights and list of publications 2021–2022

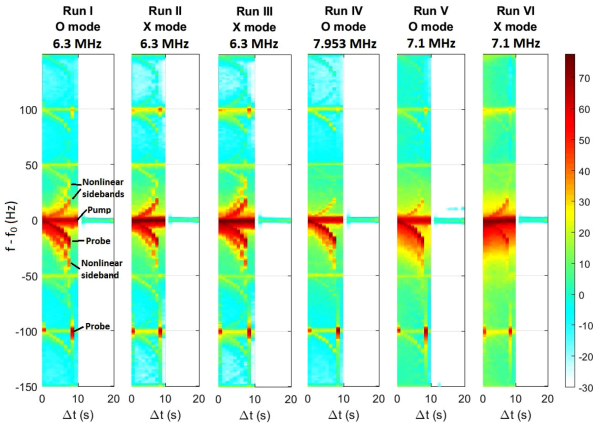

Figure 1: Spectrograms (dB) of recorded return signals in the experiment. The spectrograms are averaged over the experimental cycles. The pump signal is at $f - f_0 = 0$ and the probe is the first downshifted line at $f - f_0 = \Delta f$. Visible are several up- and downshifted sidebands attributed to nonlinear wave mixing in the ionosphere producing SEE escaping the ionospheric plasma.

Active experiments

Controlled beat-wave Brillouin scattering in the ionosphere

Eliasson et al. (2021) used EISCAT Heating to generate an ion-acoustic wave generated by the beating of an electromagnetic pump wave and a less powerful probe wave. Brillouin scattering was achieved with X and O mode polarization in the frequency range of 6.3 MHz to 7.9 MHz (Figure 1). The active control of the wave modes that are excited in the ionosphere can provide a new diagnostic for the plasma (density, composition, etc). Similarly, the natural laboratory of the ionosphere can offer insight into the physics of beat-wave interaction and other non-linear effects, relevant to laser-plasma interaction and magnetic confinement fusion.

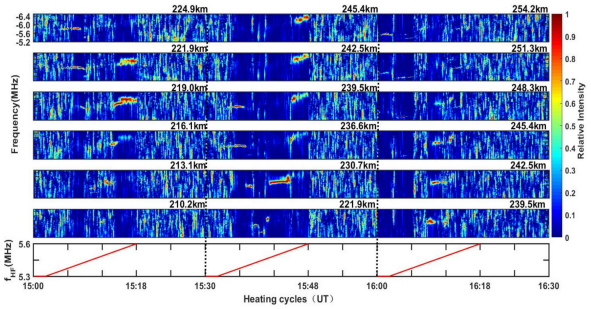

Figure 2: Downshifted plasma lines from −5.5 MHz to −6.5 MHz at different altitudes.

Studies of the high-frequency enhanced ion and plasma lines

During ionospheric heating, the high-frequency enhanced ion line (HFIL) and plasma line (HFPL) generally descend in altitude, which was previously attributed to the change in the profile of electron density. However, Wu et al. (2021) showed that those altitude descents should be dependent on the Bragg condition, and the significantly enhanced electron temperature on the travelling path plays a key role. Previous observations demonstrate consistency with the suggested theory.

With regard to the UHF observation when the pump is operating near the fourth electron gyrofrequency, Z. Li, Fang et al. (2021) suggested that the strong Langmuir turbulence in the Zakharov model cannot completely explain the outshifted plasma line, but it plays a significant role in superthermal electron. In addition, by examining HFIL and HFPL (Figure 2) induced by the alternating O mode and X mode pump, Z. Li, Li et al. (2021) found that the leakage of X mode to O mode pump can satisfy the thresholds of the parametric decay instability and the oscillation two-stream instability, and that some apparent density enhancements over a wide altitude range does not correspond to a true increase.

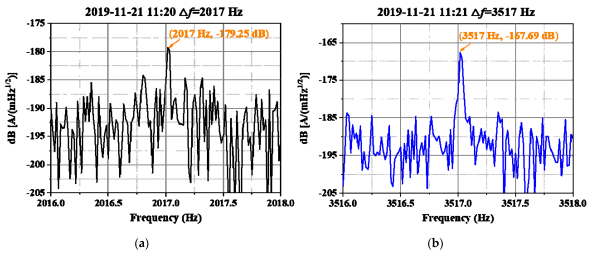

Figure 3: Amplitudes of the north-south magnetic field generated by the BW X-mode modulation heating for (a) 2017 Hz and (b) 3517 Hz.

ELF/VLF modulations of the HF signal from the EISCAT heater facility

By periodically heating the ionosphere, an electromagnetic wave in ELF (0.3 kHz to 3 kHz) and VLF (3 kHz to 30 kHz) can be radiated (Figure 3). Chen et al. (2022) showed that the X-mode and O-mode heating experiments conducted on 21 November 2019 at EISCAT indicated that the signal with the highest signal to noise ratio was measured at a frequency of 3517 Hz, rather than at 8 kHz to 12 kHz, which was measured in previous beat-wave modulation experiments.

As a potential communication technique, Yang et al. (2022) showed that the received ELF/VLF intensity was affected by the background ionosphere, and when the signal-to-noise ratio was larger than 8 dB, the bit error rate was zero, otherwise the signal-to-noise ratio and the bit error rate should satisfy the complementary error function.

GLONASS observation of artificial field-aligned plasma irregularities near magnetic zenith during EISCAT HF experiment

Sato et al. (2021) report on simultaneous observation of artificial plasma density irregularities near the magnetic zenith (MZ) by incoherent scatter radar and GNSS satellite in the high latitude (Figure 4). During an EISCAT HF heating experiment, a GLONASS satellite signal intersected the disturbed ionospheric volume along the local magnetic field lines. The satellite signal amplitude and phase were simultaneously perturbed when the electron temperature increased in the F region through O-mode HF waves. The field-aligned irregularities (FAIs) and associated density perturbations are most significantly found in the MZ direction. The growth of FAI reached the saturation level in 30 s while large-scale electron density perturbation on the order of 0.1 TECU developed in a few minutes. The observed density perturbations agree well with recent numerical studies of FAI generation due to the thermal self-focusing process.

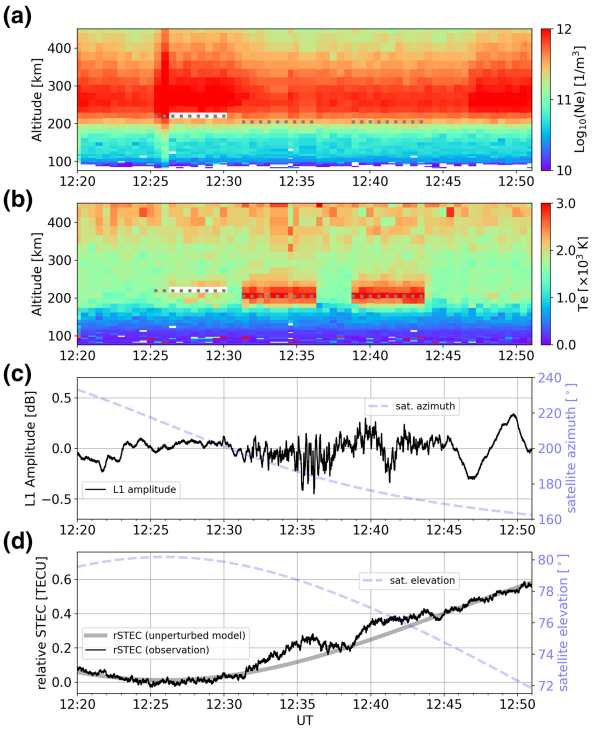

Figure 4: (a) Electron density and (b) temperature along the local magnetic field line measured by EISCAT UHF radar on 18 October 2013. The white spaces show invalid data near the reflection height. The dashed horizontal lines indicate the reflection heights. (c) GLONASS 19 L1 amplitude fluctuation. (d) Observed (black) and unperturbed (gray) relative STEC values. The satellite azimuth and elevation angles are also shown with blue dotted lines in (c) and (d), respectively. The field aligned direction is 186.2° azimuth and 77.5° elevation angle.

ELF and VLF wave modulation

In a study by Lu et al. (2021), ELF/VLF waves were modulated by quaternary phase shift keying (QPSK) and used for communication. The result demonstrates that ELF signals induced by the amplitude modulation heating of the ionosphere was successfully received by China Seismo-Electromagnetic Satellite (CSES) and the ground-based receiver, confirming that ELF/VLF waves radiated by amplitude modulation heat-

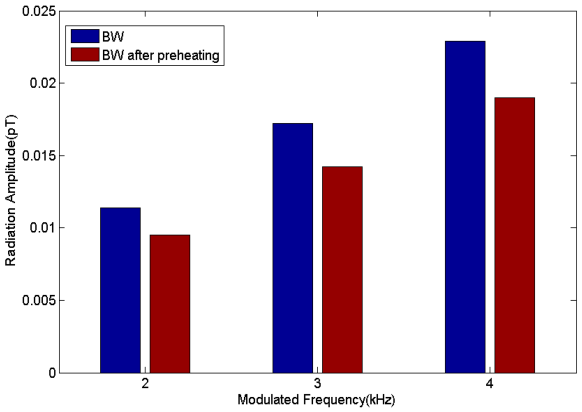

Figure 5: Simulation of signal amplitude of ELF/VLF waves generated by BW in the F region with and without preheating at different modulated frequencies received at 69.737°N, 18.896°E, about 15 km east of EISCAT.

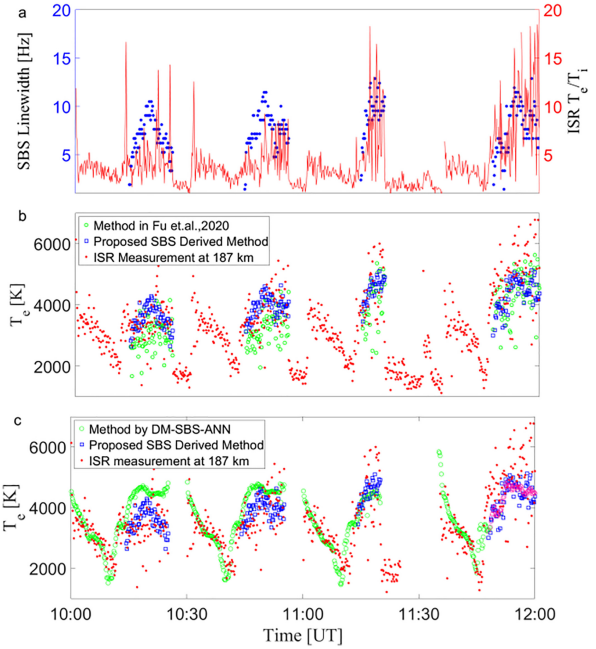

Figure 6: Comparison of extracted stimulated Brillouin scattering (SBS) linewidth (blue dot) and T_e/T_i (red line) measured by incoherent scatter radar (ISR) (a) for inversion. The T_e by the proposed SBS method (blue square) is compared with the ISR measurement and previous work in Fu et al. (2020) in panel (b). The DM-ANN inversion with SBS labeling is accomplished in panel (c) to retrieve T_e without SBS. The pink circle denotes training data and green for test data for artificial neural network.

ing of the auroral electrojet can be used for long-distance communication.

Due to the controversy of the beat-wave (BW) mechanism and the source region of the stimulated ELF/VLF waves, it is not clear whether it is an electrojet-independent method or not. Guo et al. (2021) suggested that the effect of preheating on modulation efficiency of BW based on different theories is the opposite. By supposing the opposite character of the influence and effect on the efficiency of BW in the D region and F region, a novel method was presented to identify the physical mechanism and source region of BW. This method may be feasible for solving the controversy of BW and has been verified by simulation results (Figure 5).

A stimulated emission diagnostic technique for electron temperature of the high power radio wave modified ionosphere

A stimulated electromagnetic emission (SEE), induced by high power high frequency radio waves near the third electron gyroharmonic ($3f_{ce}$), showed that stimulated Brillouin scattering spectrum (SBS) behaves similarly as spectral ion lines of the incoherent scatter radar for HF pumping frequency above $3f_{ce}$. It was also observed by Fu et al. (2022) that the SBS spectral width shows correlation with electron to ion temperature ratio. A new inversion method was proposed by incorporating the SBS spectral width within an artificial neural network approach to achieve electron temperature for ionospheric turbulent plasmas.

ISR observations of high-frequency enhanced ion and plasma lines induced by X/O mode pumping around the critical altitude

An experiment devised by Wu et al. (2022) involving alternating O/X mode pumping revealed that the high-frequency enhanced ion line (HFIL) and plasma line (HFPL) did not appear immediately after the onset of pumping, but were delayed by a few seconds. It was found that (1) the HFIL and HFPL were delayed not only in the X mode pumping but also in the O mode pumping and (2) the HFIL was not observed prior to enhancement of the electron temperature, which suggests that (1) leakage of the X mode to the O mode pumping may not be ignored and (2) spatio-

temporal uncertainties may have played important roles.

Auroral studies

Penetration of MeV electrons into the mesosphere accompanying pulsating aurorae

Pulsating aurorae (PsA) are caused by the intermittent precipitations of magnetospheric electrons (energies of a few keV to a few tens of keV) through wave-particle interactions, thereby depositing most of their energy at altitudes around 100 km. However, the maximum energy of precipitated electrons and its impacts on the atmosphere are unknown. Miyoshi et al. (2021) report unique observations by the European Incoherent Scatter (EISCAT) radar showing electron precipitations ranging from a few hundred keV to a few MeV during a PsA associated with a weak geomagnetic storm (Figure 7. Simultaneously, the Arase spacecraft has observed intense whistler-mode chorus waves at the conjugate location along magnetic field lines. A computer simulation based on the EISCAT observations shows immediate catalytic ozone depletion at the mesospheric altitudes. Since PsA occurs frequently, often in daily basis, and extends its impact over large MLT areas, it is anticipated that the PsA possesses a significant forcing to the mesospheric ozone chemistry in high latitudes through high energy electron precipitations. Therefore, the generation of PsA results in the depletion of mesospheric ozone through high-energy electron precipitations caused by whistler-mode chorus waves, which are similar to the well-known effect due to solar energetic protons triggered by solar flares.

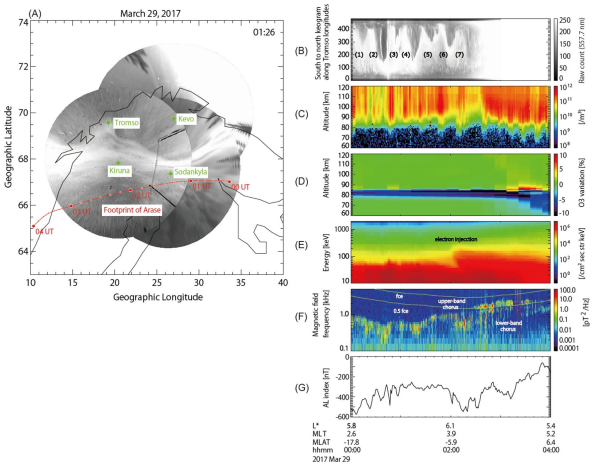

Figure 7: Geospace conditions from the upper atmosphere to the magnetosphere. (A) Map around the Scandinavian peninsula with the footprint of Arase from 00:00 UTC to 04:00 UTC on 29 March, 2017. Aurora images were obtained from the all sky imager network. (B) Keograms of an aurora image along the longitudes of Tromsø, Norway. Labels (1 to 7) show the "omega-band" structures. (C) Electron density profile from a vertical beam of the EISCAT VHF radar at Tromsø, Norway, on 29 March, 2017. The horizontal axis represents the universal time; the vertical axis denotes the altitude. The colour bar indicates the electron density. (D) Relative O_3 profile from the computer simulation based on the EISCAT observations. The colour bar indicates relative variations from the controlled run without energetic electron precipitations. (E) Energy-time diagram of electrons measured by the MEP-e/HEP/XEP instruments onboard the Arase spacecraft. The horizontal axis represents the universal time; the vertical axis denotes the electron energy. Here, MEP-e, HEP, and XEP denote the medium-energy particle—electron, high-energy particle, and extremely high-energy particle, respectively. The colour bar indicates the differential flux of electrons. (F) Frequency-time diagram of the magnetic field components of plasma waves measured by the Arase spacecraft. The vertical axis denotes the plasma wave frequency. The colour bar indicates the power spectrum density of the waves. Two lines correspond to the electron gyrofrequency (f_{ce}) and their hall frequency ($0.5 f_e$). (G) AL index.

Characteristics of Fragmented Aurora-like Emissions (FAEs) observed on Svalbard

Dreyer et al. (2021) present evidence of a new type of auroral related structure called Fragmented Aurora-like Emissions (FAEs) which they suggest are not related to direct particle precipitation (like standard auroral phenomena). Such "non particle precipitation" generated emissions have been discussed by the scientific community recently (the most well know of these being STEVE, Strong Thermal Emission Velocity enhancement). They present three case studies where FAEs were observed using All Sky Camera data (ASC) at the Kjell Henriksen Observatory (KHO) on Svalbard. A total of 305 FAE candidates were identified which the authors separated into two categories:

Type 1 Randomly occurring individual FAEs

Type 2 Wave-like structures with regular spacing between the FAEs alongside auroral arcs.

Figure 8 shows an example of Type 2 FAEs observed in ASC data. The four images indicate the apparent alignment and movement of the FAEs northwards of the main auroral arc. The authors combine the ASC images with Meridian Scanning Photometer (MSP) data as well as data from the Auroral Structure and Kinetics (ASK) instrument to investigate the emission intensities of the structures at five different wavelengths (630.0 nm, 557.7 nm and 427.8 nm from the MSP and 673.0 nm and 777.4 nm from ASK). The data indicates that the FAEs to have emissions at 630.0 nm and 557.7 nm but not at the 427.8 nm or 777.4 nm. This allows the authors to suggest an upper limit for the energy generation mechanism of 8 eV to 11 eV. ESR observations of one event indicated enhanced electron temperatures confined into a narrow altitude range in the E-region of 113 km to 119 km, co-incident with the FAEs. Enhanced ion temperatures were also observed, but at a higher altitude range, in the F-region (Figure 9).. The enhanced ion temperatures are indicative of a perpendicular electric field of around 70 mV m^{-1}, which the authors conclude is large enough to cause Farley-Buneman instabilities. They hypothesise that these instabilities could possibly cause the enhanced electron temperatures, giving rise to the emissions at 557.7 nm and 630.0 nm.

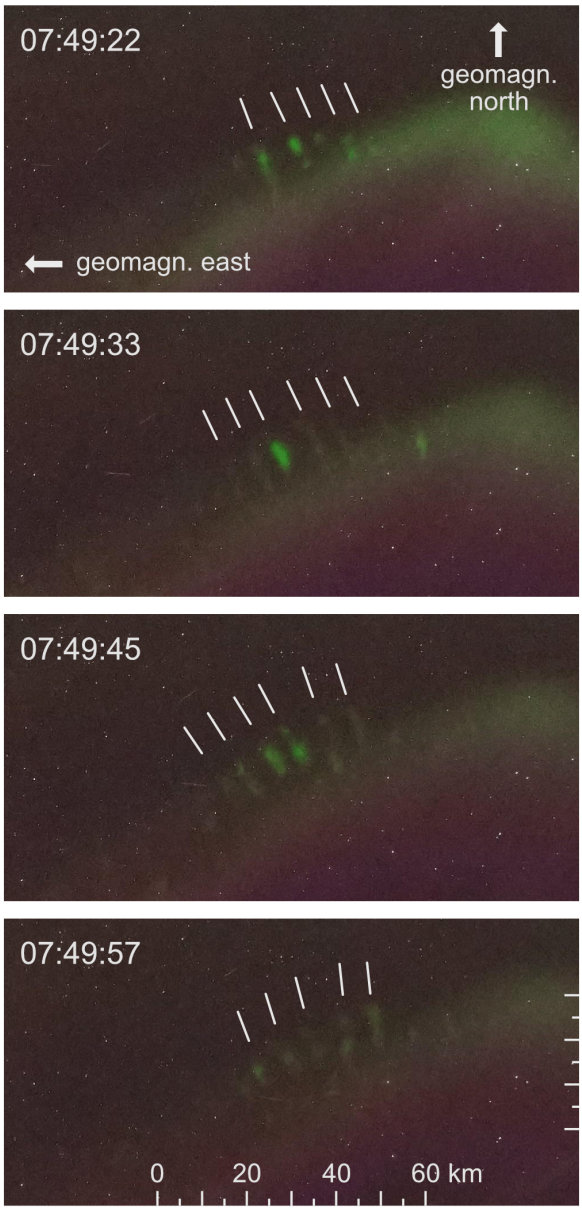

Figure 8: Movement of a Type 2 FAE group northwards of the main auroral arc over four successive images taken on 18 December 2017. White lines indicate the apparent alignment of the FAEs. The scale (in km) uses a pixel to km ratio of 0.129 (at a 65° elevation angle).

Statistical study of electron density enhancements in the ionospheric F region associated with pulsating auroras

Pulsating auroras (PsAs) are considered to be caused by energetic (more than a few keV) electron precipitation. Additionally, soft electron precipitation (less than a few keV) has often been observed in PsAs. This soft electron precipitation enhances the electron density in the ionospheric F region. However, to date, the relationship between PsAs and soft electron precipitation has not been well understood. Fukizawa et al. (2021), using the data taken by the European incoherent scatter radar and the auroral all-sky imager at Tromsø, conducted two case studies to investigate, in detail, the relationship between the electron density height profile and the type of aurora. Additionally, they conducted statistical studies for 14 events to elucidate how often F region electron density enhancement occurs with a PsA (Figure 10). They consequently found that 76 % of electron density height profiles showed a local peak in the F region, with electron temperature enhancements. It was also found that 89 % of the F region peak altitudes were above the peak altitude of the ionization rate produced by electrons of characteristic energy below 100 eV. The occurrence rate of these profiles in the hourly magnetic local time (MLT) exceeded 80 % in the 22 to 3 MLT sectors. They suggest that

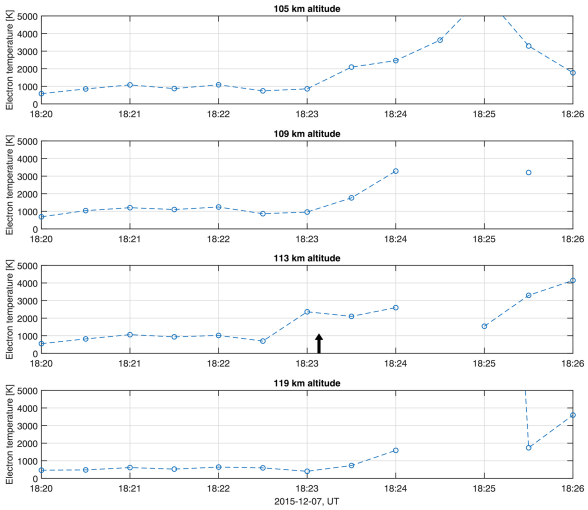

Figure 9: Time series of electron temperatures at four successive altitudes at 105 km to 119 km from incoherent scatter data from the ESR (analysed with GUISDAP) for 18:20 to 18:26 UTC on 7 December 2015. Data points with errors larger than 50 % of the values were removed. The arrow marks the time of the FAE passing and denotes the distinct increase in electron temperature specifically at 113 km.

the electron density enhancement in the F region would have been caused by electrostatic electron cyclotron harmonic waves in the magnetosphere. Another candidate would have been polar patches that had travelled from the dayside ionosphere.

Appearance and precipitation characteristics of high-latitude pulsating aurora

Characteristics of pulsating aurora (PsA) at the equatorward part of the auroral oval have been well described in the literature by previous studies. Partamies et al. (2022) extended this knowledge on high-latitude PsA observations by analysing 68 PsA events from the optical observatory on Svalbard, at 75° magnetic latitude (Figure 11). They found that the pulsating emission structures are particularly large and transient, they do not experience drift motion, or their drift motion cannot be traced. Their results showed that the high-latitude PsA events relate to lower geomagnetic activity and weaker solar wind driving than the lower latitude PsA. The high-latitude PsA events also occurred less frequently, which was in agreement with their association to lower-than-average geomagnetic activity. They further show that the ionospheric electron density values during high-latitude PsA events were low compared to the lower latitude PsA. This, together with the non-traceable nature of the pulsating emission structures, suggests that these events were strongly dominated by a sub-type called Amorphous Pulsating Aurora (APA), and the authors could therefore conclude that, unlike the lower latitude PsA events, the high-latitude PsA events were not likely to cause direct changes in the chemical composition of the mesosphere.

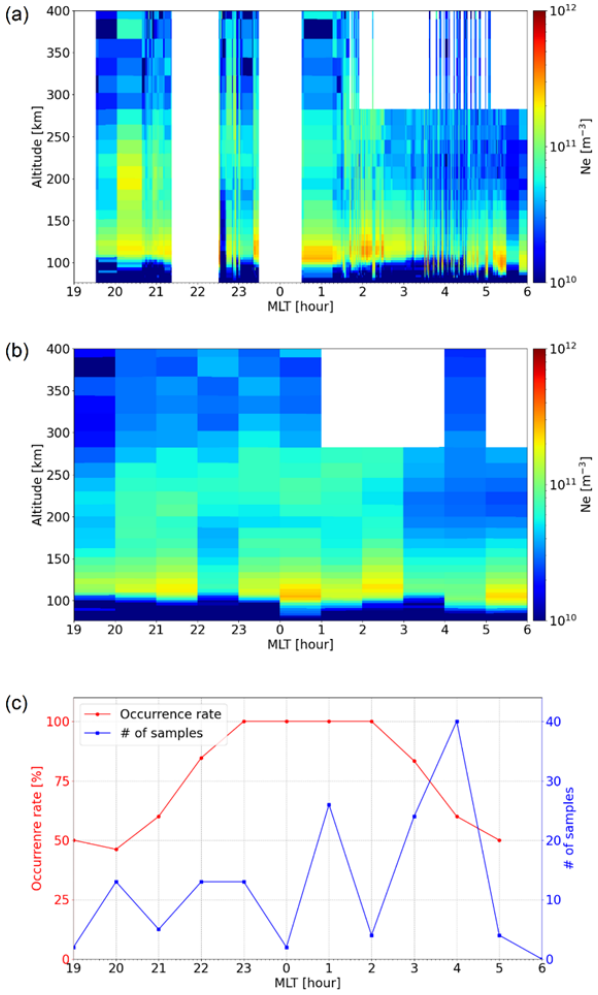

Figure 10: (a) MLT distribution of the extracted 272 electron density height profiles derived from EISCAT data. (b) Their median distribution during an hour. (c) The occurrence rate that the profile at each MLT had two peaks in the E and F region (red dot and line) and number of samples (blue dot and line).

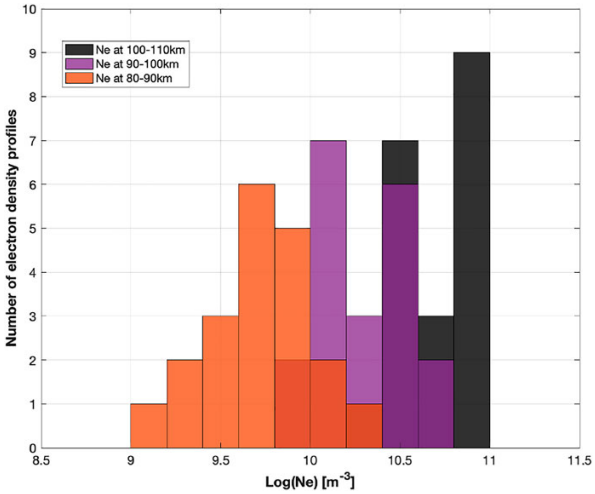

Figure 11: All available electron density (N_e) profiles during PsA events have been averaged over three height regions: 80 km to 90 km (orange), 90 km to 100 km (purple) and 100 km to 110 km (black). The bars here are transparent to show the height of the bars behind. The bin width is 0.2.

Reconstruction of precipitating electrons and three-dimensional structure of a pulsating auroral patch

In recent years, aurora observation networks using high-sensitivity cameras have been developed in the polar regions. These networks allow dimmer auroras, such as pulsating auroras (PsAs), to be observed with a high signal-to-noise ratio. Fukizawa et al. (2022) reconstructed the horizontal distribution of precipitating electrons using computed tomography with monochromatic PsA images obtained from three observation points (Figure 12). The three-dimensional distribution of the volume emission rate (VER) of the PsA was also reconstructed. The characteristic energy of the reconstructed precipitating electron flux ranged from 6 keV to 23 keV, and the peak altitude of the reconstructed VER ranged from 90 km to 104 km. They evaluated the results using a model aurora and compared the model's electron density with the observed one. The electron density was reconstructed correctly to some extent, even after a decrease in PsA intensity. These results suggest that the horizontal distribution of precipitating electrons associated with PsAs can be effectively reconstructed from ground-based optical observations.

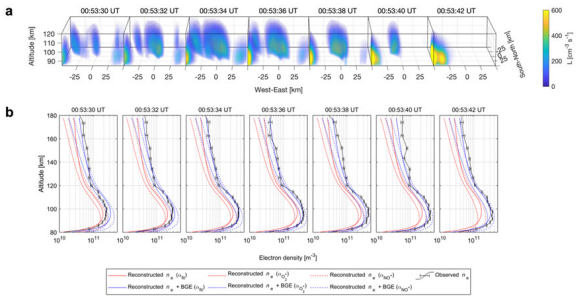

Figure 12: (a) Three-dimensional volume emission rates (L) reconstructed from auroral images with the subtraction of the background emission (BGE). (b) Electron density altitude profiles (n_e) converted from L with the BGE subtraction (red lines), those without the BGE subtraction (blue lines), and those observed by EISCAT (black lines). The measurement uncertainties are represented by error bars.

Types of pulsating aurora: comparison of model and EISCAT electron density observations

Energetic particle precipitation associated with pulsating aurora (PsA) can reach down to lower mesospheric altitudes and deplete ozone. It is well documented that pulsating aurora is a common phenomenon during substorm recovery phases. This indicates that using magnetic indices to model the chemistry induced by PsA electrons could underestimate the energy deposition in the atmosphere. Integrating satellite measurements of precipitating electrons in models is considered to be an alternative way to account for such an underestimation. One way to do this is to test and validate the existing ion chemistry models using integrated measurements from satellite and ground-based observations. By using satellite measurements, an average or typical spectrum of PsA electrons can be constructed and used as an input in models to study the effects of the energetic electrons in the atmosphere. In Tesema et al. (2022), they compared electron densities from the EISCAT radars with auroral ion chemistry and the energetics model by using pulsating aurora spectra derived from the Polar Operational Environmental Satellite (POES) as an energy input for the model (Figure 13). They found a good agreement between the model and EISCAT electron densities in the region dominated by patchy pulsating aurora. However, the magnitude of the observed electron densities suggests a significant difference in the flux of precipitating electrons for different pulsating aurora types (structures) observed.

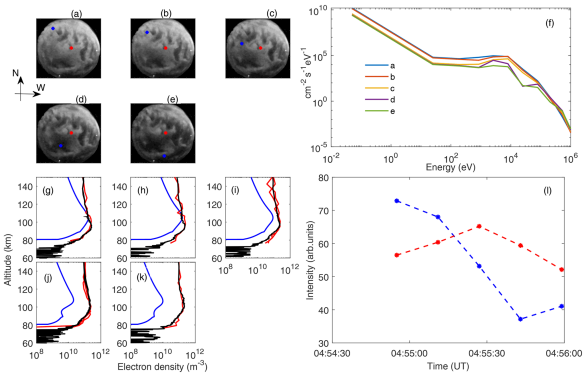

Figure 13: ASC images (a to e), with spectra constructed from POES and power law extrapolation (f). The curves labeled as a to e in panel (f) are corresponding spectra to the blue point on the ASC images, with the model (blue) and EISCAT (field aligned from UHF radar in red; zenith measurements from VHF radar in black) electron densities. Panels (g to k) correspond to the ASC images in panels (a to e), with relative auroral intensities at the location of the satellite measurements as a function of time, blue dots at POES data points corresponding to (a to e), and red dots at EISCAT.

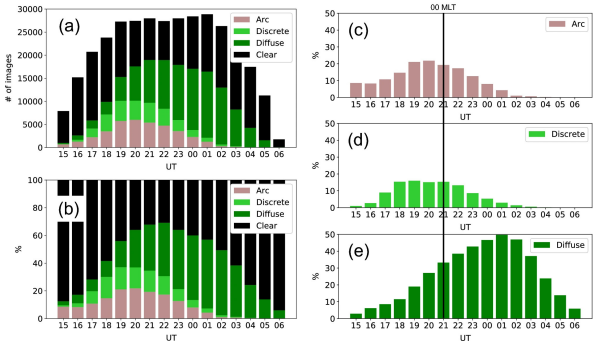

Figure 14: (a) Histogram showing the composition of images of Observable classes obtained over ten years. A decrease in the number of images in 15–18 UT and 03–06 UT is due to the difference in the the length of the dark time. (b) The composition ratio of the number of images in the Observable classes. The occurrence rate of aurora was maximum at 22 UT (01 MLT). (c)–(e) Composition ratios of panel (b) for each Auroral class. The occurrence rate of discrete auroras (Arc and Discrete) peaked before 00 MLT and was almost zero after 01 UT (04 MLT). Diffuse was most likely to occur at 01 UT (04 MLT) and the occurrence rate was widely distributed across other UTs.

An automated auroral detection system

The activity of citizen scientists who capture images of aurora borealis using digital cameras has recently been contributing to research regarding space physics by professional scientists. Auroral images captured using digital cameras not only fascinate us, but may also provide information about the energy of precipitating auroral electrons from space; this ability makes the use of digital cameras more meaningful. To support the application of digital cameras, Nanjo et al. (2022) have developed artificial intelligence that monitors the auroral appearance in Tromsø, Norway, instead of relying on the human eye, and implemented a web application, "Tromsø AI", which notifies the scientists of the appearance of auroras in real-time. This "AI" has a double meaning: artificial intelligence and eyes (instead of human eyes). Utilizing the "Tromsø AI", they also classified large-scale optical data to derive annual, monthly, and UT variations of the auroral occurrence rate for the first time. The derived occurrence characteristics are fairly consistent with the results obtained using the naked eye, and the evaluation using the validation data also showed a high F1 score of over 93 %, indicating that the classifier has a performance comparable to that of the human eye classifying observed images (Figure 14).

Comparative and combined studies

Validation of SSUSI-derived auroral electron densities: comparisons to EISCAT data

Bender et al. (2021) used FUV (far ultraviolet) (Special Sensor Ultraviolet Spectrographic Imager) SSUSI data from the DMSP F17 and F18 spacecraft to calculate ionization rates and electron density profiles in the ionospheric E-region (90 km to 150 km). These profiles were then compared to co-incident EISCAT Tromsø UHF data.

The aim of the study was to ascertain whether SSUSI data could be reliably used to calculate auroral electron density profiles of the ionospheric E-region. The database consisted of all DMSP F17 data from 2008 to 2019 and all DMSP F18 data from 2011 to 2019. For each orbit a mean electron density profile was calculated using geomagnetically mapped, pre-gridded SSUSI data points which lie in a 2° × 2° (latitude × longitude) area around the radar's geomagnetic location. These profiles were then compared to EISCAT UHF derived electron density profiles (averaged across ±5 min around the SSUSI scan time when the dish was in a high elevation, >75°, position). In total

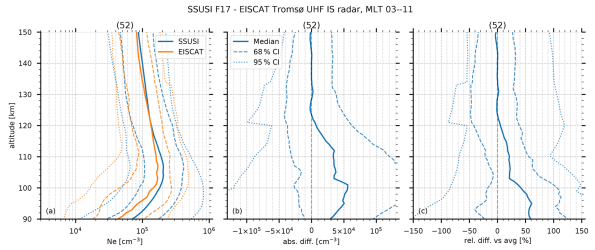

Figure 15: Profile comparison of calculated electron densities from SSUSI on DMSP F17 (in blue) and those measured by the EISCAT Tromsø UHF (orange) for the early MLT sector. Panel a indicates the density profiles whilst panels b and c show the absolute and relative differences for different confidence intervals. The numbers above the panels indicate the number of coincident satellite orbits used for averaging.

there were 537 co-incident measurements available across the morning (03–11 MLT) and evening (15–23 MLT) sectors. In the SSUSI calculations the authors assumed a Maxwellian electron distribution for the morning sector (03–11 MLT) observations and a Gaussian electron distribution in for the evening sector (15–23 MLT) observations as these provided the best fit to the EISCAT data.

Figure 15 indicate the (a) median electron density profile measured by EISCAT (orange) and SSUSI on DMSP/F17 (blue), (b) absolute differences and (c) relative differences for all morning sector observations. The solid lines represent the median values whilst the dashed (dotted) lines indicate the 68 % (95 %) confidence intervals. The authors found that, from 100 km to 150 km altitude the median of the differences varies from 0 % to 20 % and ±15 % for the F17 and F18 measurements respectively and conclude that over this altitude range SSUSI data could be used to derive reliable ionization profiles. The authors note that below this altitude range (where the density gradient becomes quite large) there is a greater difference between the two electron density profile datasets however this is generally within the 68 % confidence limit. The results indicate the possibility of providing an auroral zone database of auroral energy deposition rates using DMSP SSUSI data.

Joint Cluster/ground-based studies in the first 20 years of the Cluster mission

Fear (2022) provided a comprehensive review of the contribution that combined observations from ground-based facilities have made to the Cluster satellite mission. Measurements from the ESR

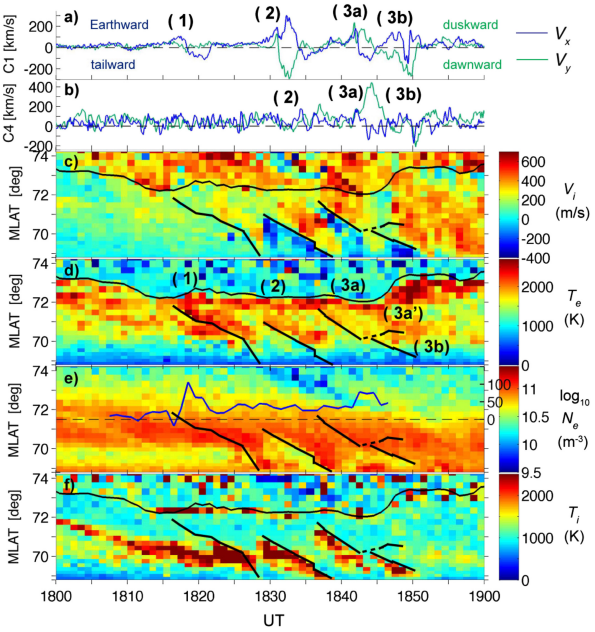

Figure 16: Cluster and European Incoherent Scatter facility VHF data, reproduced from Pitkänen et al. (2011). Panels (a and b) show the Cluster Ion Spectrometry HIA VX and VY velocity components in GSM, for Cluster 1 and 4, respectively. Panels (c to f) show the line of sight ion velocity (positive toward the radar), electron temperature, electron density and ion temperature, respectively. Bursty bulk flows are evident as positive enhancements in the VX component, observed primarily at Cluster 1. The black continuous line in panels (c, d, and f) is the estimate of the polar cap boundary, and the thicker, discontinuous black lines indicate the equatorward propagation of features which are the radar analog of auroral streamers, and associated with the earthward-propagating bursty bulk flows.

and mainland were used in conjunction with other instruments to identify signatures of dayside reconnection, polar patches, energy deposition and variations in the nightside open closed field line boundary (Figure 16).

Studies of noctilucent clouds from the stratosphere during the SONC balloon-borne experiment in 2021

Dalin et al. (2022) report a balloon-borne experiment called Stratospheric Observations of Noctilucent Clouds (SONC) which was successfully performed on the night 16–17 August 2021. A big scientific balloon, having onboard three automated cameras for studies of noctilucent clouds (NLC),

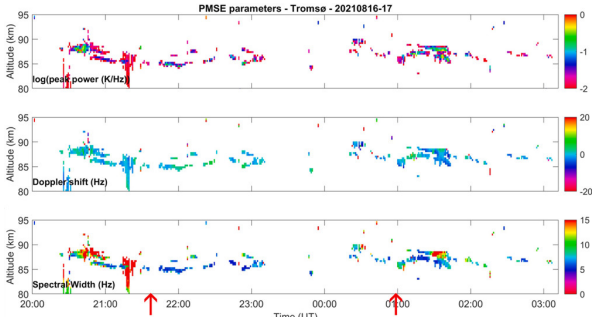

Figure 17: EISCAT 224 MHz radar measurements of PMSE parameters above Tromsø (69.58°N; 19.23°E) during the SONC balloon experiment on the night 16–17 August 2021. The upper panel shows the radar power, the middle panel is the Doppler shift and the lower panel illustrates the radar spectral width. Two red arrows show the beginning and end of the NLC observation from the stratosphere.

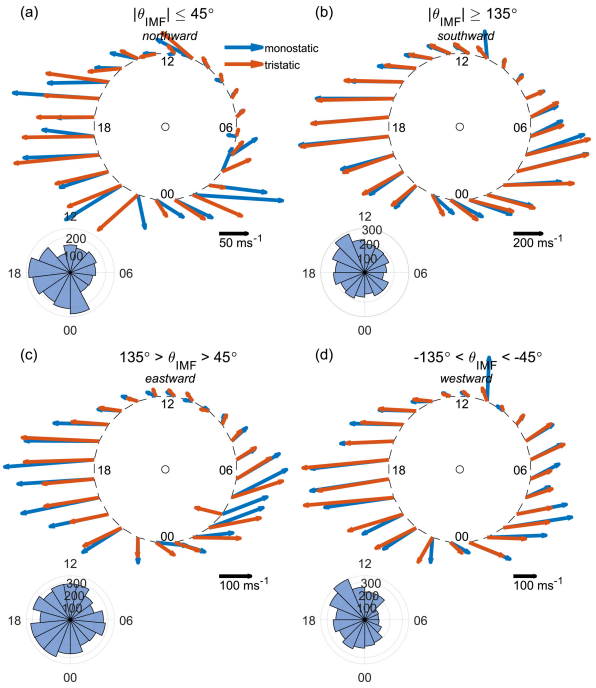

Figure 18: Clock plots showing the vectors of the weighted mean horizontal velocity in each 1-hour bin of magnetic local time (MLT) for the monostatic (blue) and tristatic (orange) measurements for different interplanetary magnetic field (IMF) conditions. The blue bar plots show the amount of data behind the averages in each bin. The single black vectors indicate the scale size for each plot. (a) northward IMF where the absolute clock angle is less than 45°; (b) southward IMF where the absolute clock angle is greater than 135°; (c) eastward IMF, with clock angle between 45° and 135°; (d) westward IMF, with clock angle between −45° and −135°. The positive (negative) clock angle is measured (anti)clockwise from north GSM. The northward IMF shows a lot of difference between the techniques, notably in angle as well as magnitude. Note that the absolute magnitude differences are similar in each plot.

was launched to 32.7 km altitude from Esrange (northern Sweden). All three NLC cameras and electronics were completely operational in the stratosphere for more than 10 h at low temperatures of about −30 °C. Two wide angle cameras registered an extended NLC field of about 1700 km long in the twilight sky sector from the north-west to the north-east of Esrange. NLC were of a moderate brightness and were located at high latitudes between 68°N and 71°N. The NLC field was located in a cold area (138 K to 142 K) below the frost point temperature (145 K to 148 K) in the mesopause region that was confirmed by Aura/MLS satellite and Esrange lidar measurements. The balloon-borne NLC measurements were accompanied by ground-based lidar and radar measurements (Figure 17). The latter have registered Polar Mesosphere Summer Echoes (PMSE) in the same volume of the summer mesopause along with NLC observed from the stratosphere that has been performed for the first time above northern Scandinavia. They describe the technique and method of the NLC observation from the stratosphere as well as present the first scientific results of the SONC experiment.

Two techniques for determining F-region ion velocities at meso-scales: Differences and impacts on Joule heating

Kavanagh et al. (2022) used the archive of EISCAT Common Programme 2 (CP2) data to compare and contrast the estimated ion velocities derived from the monostatic and tristatic techniques. They found that although the overall statistics and large scale response to solar wind driving were very similar, differences do occur under strongly northward IMF conditions, when local turbulent flow may dominate (Figure 18). At small scales the difference between the two techniques is well correlated with the inherent variability in the tri-static measurement suggesting an impact of small scale flow bursts. Estimates of Joule Heating from the two methods show considerable differences that depend on magnetic local time and geomagnetic activity levels.

Multi-Point Measurements of the Plasma Properties Inside an Aurora From the SPIDER Sounding Rocket

The Small Payloads for Investigation of Disturbances in Electrojet by Rockets (SPIDER) sounding rocket was launched on 2 February, 2016 (21:09 UT), deploying 10 free falling units (FFUs) inside a westward traveling auroral surge. Each FFU deployed spherical electric field and Langmuir probes on wire-booms, providing in situ multipoint recordings of the electric field and plasma properties. The analytical retrieval of the plasma parameters, namely the electron density, electron temperature and plasma potential, from the Langmuir probe measurements was non-trivial due to sheath effects and detailed explanation are discussed by Giono et al. (2021). An empirical assumption on the sheath thickness was required, which was confirmed by simulating the plasma environment around the FFU using the Spacecraft Plasma Interaction Software (SPIS). In addition, the retrieved electron density and temperature are also in agreement with the simultaneous incoherent scatter radar measurements from the EISCAT facility (Figure 19). These two independent confirmations provided a good level of confidence in the plasma parameters obtained from the FFUs, and events observed during the flight are discussed in more details. Hints of drift-wave instabilities and increased currents inside a region of enhanced density were observed by the FFUs.

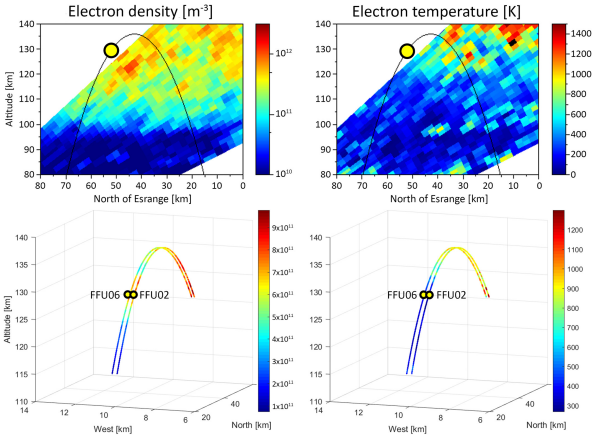

Figure 19: Snapshot of the electron density (left panels) and electron temperature (right panels) recorded by EISCAT along the upleg part of the trajectory (top panels) and by the free falling units (FFUs) along the down-leg part of the trajectory (bottom panels). The yellow dots show the position of the FFUs at the time of the EISCAT measurement.

Dual frequency measurements of meteor head echoes simultaneously detected with the MAARSY and EISCAT radar systems

Schult et al. (2021) present dual frequency measurements of common meteor head echoes, conducted with the VHF radar MAARSY (53.5 MHz) and the UHF EISCAT (930 MHz) radar located in Northern Norway (Figure 20). With temporal resolutions of 1 ms, they find most head echoes show a continuous increase/decrease in radar cross section (RCS) with time at both frequencies. In some cases, a sudden drop of several dBsm is detected by both radars, which they interpret as direct evidence for gross fragmentation. The mean difference of the RCS between both frequencies is about 17 dBsm at an average altitude of 100 km. Schult et al. (2021) find a clear positive correlation between both RCS's as well as a trend of RCS increasing with altitude. All of their detected meteor head echoes followed cometary-type orbits prior to Earth impact.

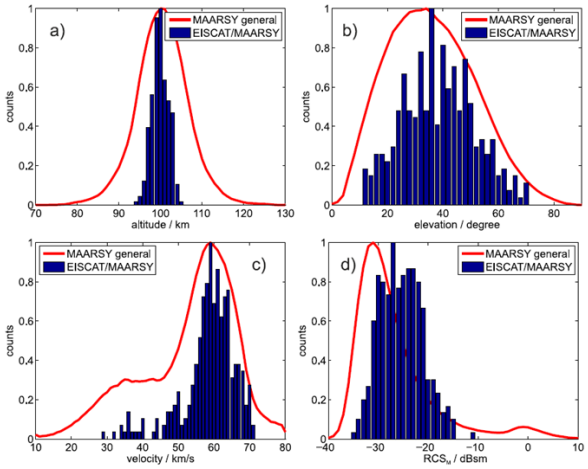

Figure 20: Overview of the meteor properties ((a) mean detection altitude, (b) trajectory entry angle, (c) mean velocity and (d) mean radar cross section) observed simultaneously with MAARSY and EISCAT (blue bars). For comparison the red lines show the general distribution observed with MAARSY.

Plasma neutral gas interactions in various space environments: Assessment beyond simplified approximations as a Voyage 2050 theme

Yamauchi et al. (2022) prepared a White Paper in response to the European Space Agency (ESA) Voyage 2050 Call. They present the importance of advancing our knowledge of plasma-neutral gas interactions, and of deepening our understanding of the partially ionized environments that are ubiquitous in the upper atmospheres of planets and moons, and elsewhere in space. In future space missions, the above task requires addressing the fundamental questions: (A) How and by how much do plasma-neutral gas interactions influence the re-distribution of externally provided energy to the composing species? (B) How and by how much do plasma-neutral gas interactions contribute toward the growth of heavy complex molecules and biomolecules? A large advantage for terrestrial missions because of strong support from remote sensing measurements by ground-based instruments, including EISCAT_3D, is pointed out.

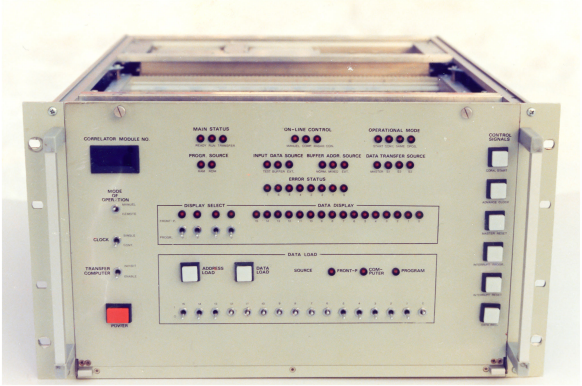

Figure 21: The arithmetic unit of one of the Alker correlators. The front panel layout has many features reminiscent of minicomputers of the 1970s era, in particular the "data load" field with 16 switches to set up and manually load individual micro-instructions into arbitrary program memory locations; the front panel of the Nord-10 computer had an almost identical field for the same purpose. Photo courtesy of Lars-Göran Vanhainen.

EISCAT and EISCAT_3D

History of EISCAT — Part 5: Operation and development of the system during the first two decades

Wannberg (2022) gives an inside view of the first twenty years of operation of the Kiruna-Sodankylä-Tromsø (KST) part of EISCAT as experienced and remembered by him. The paper is subdivided into an Introduction and 14 additional sections describing the organisation, staffing and responsibilities of the sites, with particular emphasis on the transmitter-related work at Tromsø and the commuting of staff and equipment between the sites. Also the headquarters operation and UHF and VHF radar systems are treated including a summary of transmitter and antenna problems not available elsewhere in easily accessed media. The computer system and the proprietary control languages EROS, TARLAN and CORLAN are described as well as the signal processing hardware, with special emphasis on the Alker correlator (Figure 21), its idiosyncrasies and the gradual unlocking of its capabilities through UNIPROG, the GEN system and the G2 system, culminating in the ability to run alternating code experiments routinely. The time and frequency keeping was a non-trivial task in the early 1980s. Finally, the UHF spectrum problem is discussed which relates how the UHF system had to be constantly upgraded in order to be able to co-exist with the emerging mobile phone networks until the final closure of UHF reception at Kiruna and Sodankylä in 2012.

Observing electric field and neutral wind with EISCAT_3D

Stamm, Vierinen and Gustavsson (2021) presented an investigation into the feasibility of using the new EISCAT_3D (E3D) system to estimate the 3D electric field and neutral wind velocity along a magnetic field aligned profile, using the 3D ion velocity measurements and a newly proposed method. In comparison to previous methods, their method does not assume that the electric field is constant along the magnetic field line but rather uses Maxwell's equations, in combination with the ion momentum equation to provide additional constraints to the derived E-field and neutral wind. The model uses the E3D frequency of 223 MHz, a one-way half power beam width of 2°, a transmitter and receiver gain of 38 dB, transmitter power of 5 MW and a noise temperature of 200 K (parameters consistent with the E3D system). They ran the model for three different ionospheric conditions: day-time, night-time with au-

roral precipitation and night-time without auroral precipitation (quiet time). The ionospheric profiles during times of auroral precipitation are provided by EISCAT UHF data for 20 February 2014 whilst the daytime and quiet time data are taken from the corresponding IRI model. The model data are then integrated over 10 min. The authors also incorporate data from the Joule II rocket campaign to provide suitable constraints of various model parameters in regard to the variation of the electric field and neutral wind with altitude.

Figure 22 shows the 1σ uncertainties for both the electric field (top row) and neutral wind (bottom row) estimates for different ionospheric conditions and model parameter constraints. The ionospheric conditions are indicated with different line styles with a solid line for daytime, dashed line for night time without aurora and the dashed-dotted lines for night time with aurora. The different colours related to the different model parameter constraints. For example, in the case of the electric field (top row) the yellow (α*0.1) and blue (α*0.001) profiles are generated assuming horizontal gradients of the electric field to be a factor of 10 or 1000 smaller in magnitude than those used to generate the cyan profile (α*1.0). The authors find that, during favourable ionospheric conditions the ion velocity at the E-region peak can be measured with an accuracy of less than 1 m s^{-1}, however, during geomagnetically quiet times this uncertainty can increase by a factor of 10. The neutral wind estimates in the lower E-region, during favourable conditions, have a standard deviation of less than 10 m s-1. Under these conditions the F-region electric field can be estimated with an uncertainty of 1 mV m^{-1}.

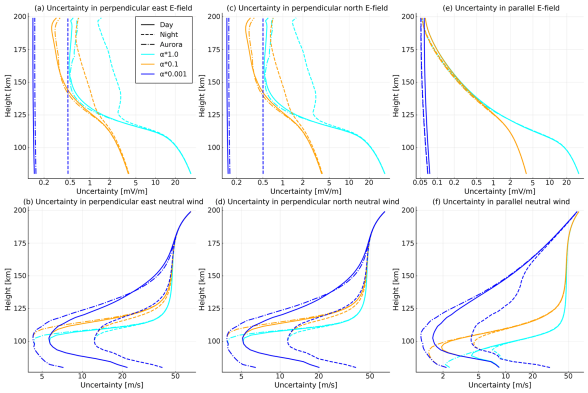

Figure 22: 1σ uncertainty of estimates of electric field (top row) and neutral wind (bottom row). Daytime profiles are shown in solid lines and night time profiles with and without aurora are shown with dashed and dashed-dotted lines respectively. The different colours relate to the different parameterization constraints used in the model.

Radar observability of near-Earth objects using EISCAT_3D

Kastinen et al. (2020) modeled how radar observations can be used to obtain accurate orbital elements for near-Earth objects (NEOs) as a result of the very accurate range and range rate measureables. These observations allow the prediction of NEO orbits further into the future and also provide more information about the properties of the NEO population. This study evaluates the observability of NEOs with the EISCAT_3D 233 MHz 5 MW high-power, large-aperture radar, which is currently under construction. Three different populations are considered, namely NEOs passing by the Earth with a size distribution extrapolated from fireball statistics, catalogued NEOs detected with ground-based optical telescopes and temporarily captured NEOs, i.e. mini-moons. Two types of observation schemes are evaluated, namely the serendipitous discovery of unknown NEOs passing the radar beam and the postdiscovery tracking of NEOs using a priori orbital elements. The results indicate that 60 to 1200 objects per year, with diameters D>0.01 m, can be discovered (Figure 23). Assuming the current NEO discovery rate, approximately 20 objects per year can be tracked post-discovery near the closest approach to Earth. Only a marginally smaller number of tracking opportunities are also possible for the existing EISCAT ultra-high frequency (UHF) system. The mini-moon study, which used a theoretical population model, orbital propagation, and a model for radar scanning, indicates that approximately seven objects per year can be discovered using 8 % to 16 % of the total radar time. If all mini-moons had known orbits, approximately 80 to 160 objects per year could be tracked using a priori orbital elements. The results of this study indicate that it is feasible to perform routine NEO post-discovery tracking observations using both the existing EISCAT UHF radar and the upcoming EISCAT_3D radar. Most detectable objects are within one lunar distance (LD) of the radar. Such observations would complement the capabilities of the more powerful planetary radars that typically observe objects further away from Earth. It is also plausible that EISCAT_3D could be used as a novel type of an instrument for NEO discovery, assuming that a sufficiently large amount of

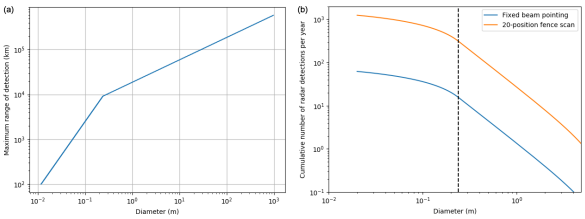

Figure 23: Panel (a) Maximum range at which an object of a certain diameter is detectable with E3D with a 0.2 s coherent integration length. The range grows initially faster due to object sizes being in the Rayleigh scattering regime, where the radar cross section grows proportionally to $\sigma \propto D^6$, and where D is object diameter. Once the transition to geometric scattering occurs, the maximum detectable range grows more slowly. Panel (b) The estimated cumulative number of radar detections per year with E3D, assuming 100 % time use. The blue line is without beam scanning, and the orange line is with a 20-position fence scan. The black broken line indicates the transition from Rayleigh to geometric scattering.

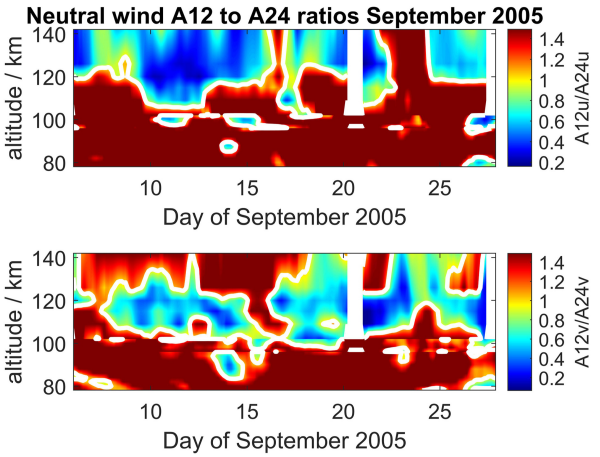

Figure 24: Ratio of semidiurnal to diurnal amplitudes in zonal (top) and meridional (bottom) neutral winds. The meridional component shows a two-band structure of dominant semidiurnal oscillations.

radar time can be used. This could be achieved, for example by time-sharing with ionospheric and space-debris-observing modes.

Ionospheric variations

Determining the origin of tidal oscillations in the ionospheric transition region with EISCAT radar and global simulation data

At high-latitudes, diurnal and semidiurnal variations of temperature and neutral wind velocity can originate both in the lower atmosphere (UV or infrared absorption) and in the thermosphere-ionosphere (ion convection, EUV absorption). Determining the relative impact of different forcing mechanisms gives insight to the vertical coupling in the ionosphere. Günzkofer et al. (2022) analyze measurements from the incoherent scatter radar (ISR) facility operated by the EISCAT Scientific Association. They are complemented by meteor radar data and compared to global circulation models. The amplitudes and phases of tidal oscillations are determined by an adaptive spectral filter (ASF). Measurements indicate the existence of strong semidiurnal oscillations in a two-band structure at altitudes less than about 110 km and at larger than about 130 km, respectively (Figure 24). Analysis of several model runs with different input settings suggest the upper band to be forced in situ while the lower band corresponds to upward-propagating tides from the lower atmosphere. This indicates the existence of an unexpectedly strong, in situ forcing mechanism for semidiurnal oscillations in the high-latitude thermosphere. It is shown that the actual transition of tides in the altitude region from 90 km to 150 km is more complex than described so far.

Thermospheric wind response to a sudden ionospheric variation in the trough

Oyama et al. (2022) studied the thermospheric wind response to a sudden westward turning of the ion velocity at a high latitude by analyzing data obtained with a Fabry–Perot interferometer (FPI; 630 nm), Dynasonde, and the Swarm A and C satellites during a conjunction event (Figure 25). The event occurred during a geomagnetically quiet period ($\mathrm{Kp} = 0+$) through the night, but some auroral activity occurred in the north. The collocated FPI and Dynasonde measured the thermospheric wind ($\mathbf{U}$) and ionospheric plasma velocity ($\mathbf{V}$), respectively, in the F region at the equatorward trough edge. A notable scientific message from the study is the possible role of thermospheric wind in the energy dissipation process at F region altitude. The FPI thermospheric wind did not instantly follow a sudden $\mathbf{V}$ change due to thermospheric inertia in the F region. At a pseudo-breakup during the event, $\mathbf{V}$ suddenly changed direction from east-

ward to westward within 10 min. **U** was concurrently accelerated westward, but its development was more gradual than that of **V**, with **U** remaining eastward for a while after the pseudo-breakup. The delay of **U** is attributed to the thermospheric inertia. During this transition interval, $\mathbf{U} \cdot \mathbf{V}$ was negative, which would result in more efficient generation of frictional heating than the positive $\mathbf{U} \cdot \mathbf{V}$ case. The sign of $\mathbf{U} \cdot \mathbf{V}$, which is related to the relative directions of the neutral wind and plasma drift, is important because of its direct impact on ion-neutral energy exchange during collisions. This becomes especially important during substorm events, where rapid plasma velocity changes are common. The sign of $\mathbf{U} \cdot \mathbf{V}$ may be used as an indicator to find the times and locations where thermospheric inertia plays a role in the energy dissipation process.

An EISCAT UHF/ESR experiment that explains how ionospheric irregularities induce GPS phase fluctuations at auroral and polar latitudes

John, Forte, Astin, Allbrook, Arnold, Vani, Häggström and Sato (2021) conducted an experiment using the UHF and ESR to characterise the effect of electron density irregularities on temporal fluctuations in Total Electron Content, in coordination with ground GNSS receivers. The results (Figure 26) indicate that fluctuations in TEC produced by polar plasma patches and particle precipitation have similar temporal scales. This places an intrinsic limitation on the monitoring and tracking of plasma patches via ground GNSS observations.

On the relationship of energetic particle precipitation and mesopause temperature

Energetic particle precipitation (EPP) has the potential to change the neutral atmospheric temperature in the mesopause region. However, recent results are inconsistent, leaving the mechanism and the actual effect still unresolved. In a study, Enengl et al. (2021) searched for electron precipitation events and investigated a possible correlation between D-region electron density enhancements and simultaneous neutral temperature changes. The rotational temperature of the excited hydroxyl (OH) molecules is retrieved from the infrared spectrum of the OH airglow.

The electron density was monitored by the European Incoherent Scatter Scientific Association

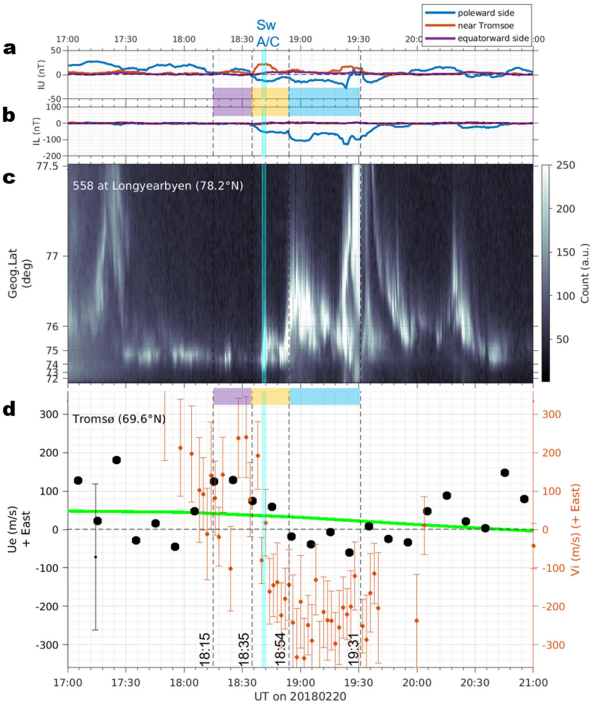

Figure 25: Time series of (a) IU, (b) IL, (c) keogram made of the all-sky camera at Longyearbyen (but from 72°N to 77.5°N) and (d) zonal component of the FPI-measured neutral wind (black dots) and ion velocity from the Dynasonde (orange dots) at Tromsø from 17 to 21 UT on 20 February 2018. Post-integration of four FPI fringe images was applied, corresponding to a 10 min time resolution. The mean error of the neutral wind for the selected four hours is illustrated by a black vertical bar. Individual errors of the ion velocity are marked by orange vertical bars. The green curve represents the HWM zonal wind at 250 km altitude. The time of the Swarm pass over Scandinavia is marked by a vertical light blue bar, which is drawn from 18:40:18 to 18:42:08 UT, corresponding to the shifted geographical latitude from 67°N to 74°N. The time interval from 18:15 to 19:31 UT is separated into three groups, highlighted in purple, yellow, and light blue.

(EISCAT) Svalbard Radar. Enengl et al. (2021) used all available experiments from the International Polar Year (IPY) in 2007–2008 until February 2019. Particle precipitation events are characterized by rapid increases in electron density by a factor of 4 at an altitude range of 80 km to 95 km, which overlaps with the nominal altitude of the infrared OH airglow layer. The OH airglow measurements and the electron density measurements are co-located. Six of the ten analysed electron precipitation events are associated with a temperature

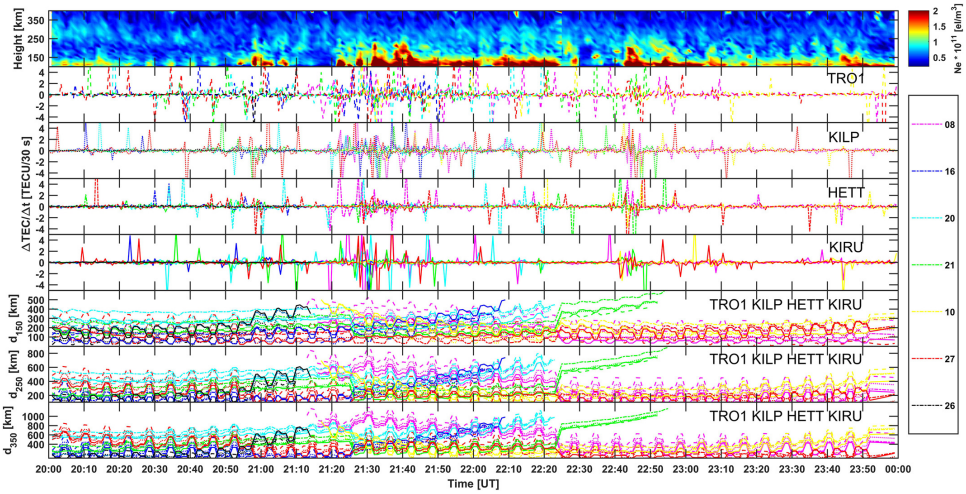

Figure 26: EISCAT profiles of electron density as function of height; 30 s Global Positioning System (GPS) TEC fluctuations from Tromsø (TRO1, dashed lines), Kilpisjärvi (KILP, dotted lines), Hetta (HETT, dash-dotted lines), and Kiruna (KIRU, solid lines) for GPS PRNs 08 (magenta), 16 (blue), 20 (cyan), 21 (green), 10 (yellow), 27 (red), and 26 (black); separation distances d_{150}, d_{250}, and d_{350} between ionospheric pierce points of EISCAT beams and GPS ray paths at 150 km, 250 km and 350 km shell height, respectively between 20:00 UT and 24:00 UT on March 15, 2018. These separation distances were estimated for all the GNSS ground stations considered (i.e., TRO1, KILP, HETT, and KIRU).

decrease of 10 K to 20 K. Four events were related to a temperature change of less than 10 K.

They interpret the results in terms of the change in the chemical composition in the mesosphere. Due to EPP ionization the population of excited OH at the top of the airglow layer may decrease. As a consequence, the airglow peak height changes and the temperatures are probed at lower altitudes. The observed change in temperature thus depends on the behaviour of the vertical temperature profile within the airglow layer. This is in agreement with conclusions of earlier studies but is, for the first time, constructed from electron precipitation measurements as opposed to proxies. The EPP-related temperature change recovers very fast, typically within less than 60 min (Figure 27). They therefore further conclude that this type of EPP event reaching the mesopause region would only have a significant impact on the longer-term heat balance in the mesosphere if the lifetime of the precipitation was much longer than that of an EPP event (30 min to 60 min) found in this study.

Low-altitude ion upflow observed by EISCAT and its effects on supply of molecular ions in the ring current detected by Arase (ERG)

During the magnetic storm starting on 7 September 2017, the MEP-i instrument onboard the Arase (ERG) satellite observed molecular ions ($O_2^+/NO^+/N_2^+$) in the ring current. The molecular ions were observed by Arase in four orbits during this magnetic storm. This indicates that there was a continuous molecular ion supply from the ionosphere. During the storm main phase around the second Dst minimum (around −100 nT) on 8 September, 2017, the European Incoherent Scatter (EISCAT) radar observed the ion upflow (around 50 m s^{-1} to 150 m s^{-1}) in the low-altitude (250 km to 350 km) ionosphere together with strong ion heating up to more than 2000 K (Figure 28). The convective electric field derived from the electron heating observed by EISCAT at an altitude of approximately 110 km was also enhanced by a factor of two. The observations suggest that the additional ion heating at low altitudes helps to cause the fast upflow and transport molecular ions upward. The flux decreases from 280 km to 350 km altitudes due to the dissociative recombination was estimated to be approximately two orders of magnitude. This resulted in significant molecular ion flux remaining at 350 km alti-

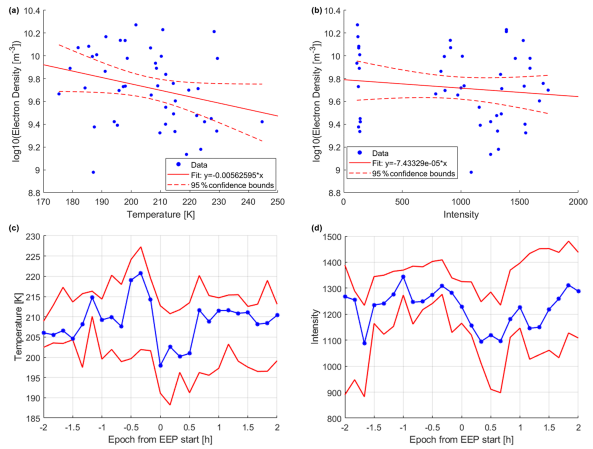

Figure 27: Illustration the average temperature and intensity response to the EPP onset. Panels (a) and (b) show scatter plots of the electron density and the airglow temperature (intensity) values, including data points from half an hour before to 1 h after the EPP event for the six decreasing events. The regression line with its 95 % confidence bounds is shown in red. The superposed epoch of the airglow temperature in panel (c) (airglow intensity in panel (d)) includes the 25th (lower red line), 50th (blue) and 75th (upper red line) percentiles of the temperature for all ten events. The first and second events are accompanied by very low-intensity values. To reduce the dominance of these two events, the lower percentile for intensity is set at 35 %. The zero epoch time corresponds to the EPP onset. The measurements are chosen closest to the respective epoch time and averaged. Each 30 min epoch time bin contains 6 to 10 temperature (intensity) values. The variation in the number of data points is due to individual missing data points.

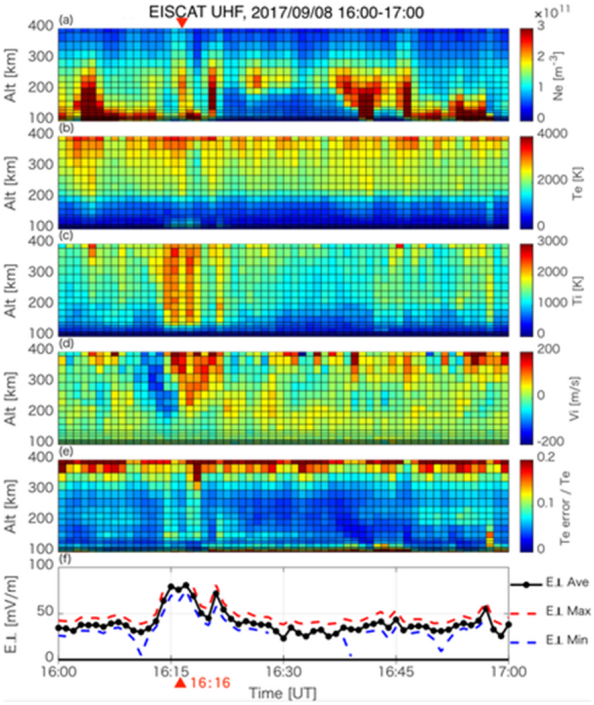

Figure 28: EISCAT observations from 16 UT to 17 UT on 8 September, 2017. From top to bottom, each panel shows (a) electron density, (b) electron temperature, (c) ion temperature, (d) ion velocity, (e) error ratio of electron temperature, and (f) electric field perpendicular to the magnetic field derived from electron heating at 111 km altitude based on empirical relations.

tude. These results suggest that the low-altitude ion upflow caused by the ion frictional heating enables molecular ions to escape to space against rapid loss by the dissociative recombination.

Solar flare effects in the Earth's magnetosphere

The solar wind has major impacts on the Earth's magnetosphere, but it is unclear whether the same holds for solar flares. Liu et al. (2021) used a recently developed full geospace model, combined with observational data from the 6 September 2017 X9.3 solar flare event (Figure 29), to reveal solar flare effects on the magnetospheric dynamics and on the electrodynamic coupling between the magnetosphere and its adjacent ionosphere. A rapid and large increase was observed in flare-induced photoionization of the polar ionospheric E region at altitudes from 90 km to 150 km. This reduces the efficiency of mechanical energy conversion in the dayside solar wind-magnetosphere interaction, resulting in less Joule heating of the Earth's upper atmosphere, a reconfiguration of magnetosphere convection, as well as changes in dayside and nightside auroral precipitation. It was thus demonstrated that solar flare effects extend throughout the geospace via electrodynamic coupling, and are not limited, as previously believed, to the atmospheric region where radiation energy is absorbed.

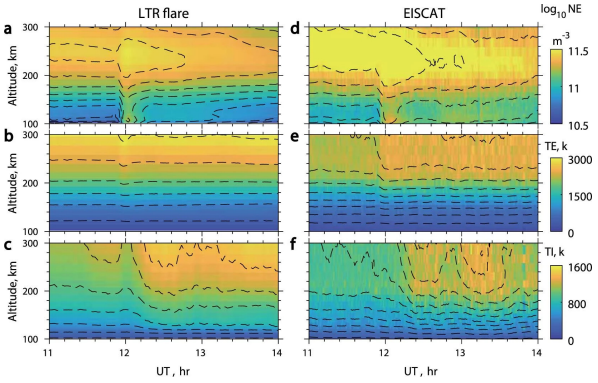

Figure 29: Universal time and altitude variations of electron density (N_e), electron temperature (T_e), and ion temperature (T_i) from LTR flare simulations (left panels) and EISCAT Tromsø VHF radar (right panels) on 6 September 2017. Since the VHF radar was pointing at geographic north with 30° elevation angle, the latitudinal coverage is about 69° to 72° for 80 km to 400 km altitude.

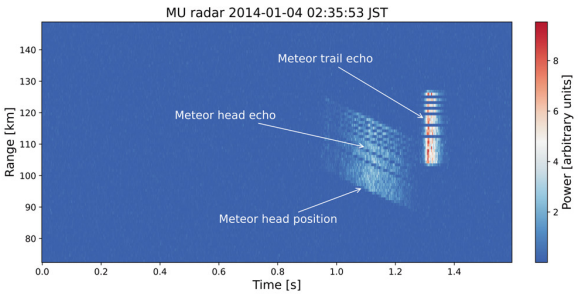

Figure 30: Range-time intensity plot of the output voltage data generated by the MU radar. The time of the first radar pulse in the figure title is given in Japan Standard Time (JST).

Methodology

A hybrid MPI/OpenMP parallelization scheme based on nested FDTD for parametric decay instability

Simulating Parametric decay instability (PDI) is time-consuming and difficult due to the high spatial resolution and strict restriction on the discrete time step. A hybrid Message Passing Interface (MPI)/OpenMP parallelization scheme was used by Fu et al. (2022) to solve the above-mentioned problems, reducing the 70 h of simulation time to 3.6 h.

From meteors to space safety: Dynamical models and radar measurements of space objects

In his PhD thesis Daniel Kastinen (Kastinen, 2022) developed an automated radar data analysis algorithm for meteor head echo measurements. The analysis algorithm is able to produce realistic uncertainties for each individual meteor event, including the meteoroid orbit. Many of the resulting probability distributions are non-Gaussian, which needs to be accounted for. The analysis algorithm was applied to interferometric high-power large-aperture MU radar data in a case study on high altitude meteors (Figure 30). The study found that 74 out of 106 000 meteors appeared higher than 130 km and a few confirmed detections reached up to 150 km altitude.

Comet 21P/Giacobini–Zinner is the parent body of the meteoroid stream giving rise to the October Draconid meteor shower. The meteoroid stream was simulated accounting for parent body orbital uncertainties to estimate meteor shower parameters. The simulation was able to model the unexpected mass distribution observed in the 2011 and 2012 October Draconids. It also successfully predicted a meteor outburst in 2018. Further, methods to reduce the computation time of meteoroid stream simulations using importance sampling were derived and implemented on a test model.

EISCAT radar measurements were performed to study space debris from the Kosmos-1408 satellite, which had been destroyed and fragmented in orbit on 15 November, 2021. A novel method to estimate the size distribution of debris objects was developed. Data from two EISCAT radars were used to demonstrate a new initial orbit determination technique, yielding good agreement with known catalogue orbits. Finally, the detectability of near-Earth objects (NEOs) with the EISCAT_3D radar currently under construction was simulated. It was predicted that as many as seven temporarily captured NEOs, i.e. minimoons, could be discovered per year depending on the amount of allocated observation time. The predictions also show that hundreds of NEOs could be tracked yearly to improve their orbits.

An improved iterative algorithm utilised in data processing for incoherent scatter radar

The Levenberg–Marquardt (LM) method is a widely used algorithm for nonlinear iteration in modern incoherent scatter radar (ISR) data processing. In a study by Xiong et al. (2022) a new iteration algorithm, the so-called dog leg (DL) method, was introduced. By comparing their performance, it was shown that the DL method has better accuracy and iteration speed than that of the LM method. In addition, the error of the DL method is more stable than that of the LM method. Moreover, the DL method is more convergent than the LM method, which helps avoid the lack of ionospheric parameter due to the divergence of iteration with the LM method.

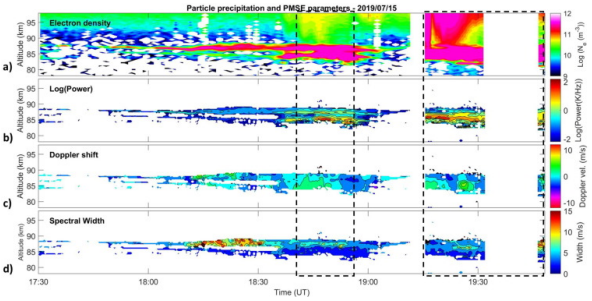

Figure 31: Observations on 15 July 2019 after applying the noise removal threshold conditions to the Gauss fitting outputs of the spectrum. Note that almost all noise except PMSE are removed. (a) Electron density estimates using GUISDAP for which the noise thresholds we mentioned did not apply, (b) log(Power (K/Hz)), (c) Doppler velocity (m/s) and (d) Spectral width (m/s). The dashed box shows durations of particle precipitation reaching below 90 km.

Polar mesospheric summer and winter echoes

Effects of particle precipitation on the polar mesospheric summer echoes observed by the EISCAT VHF radar

Narayanan et al. (2022) presented the results from an investigation of spectra of polar mesospheric summer echoes (PMSE) observed with the EISCAT VHF 224 MHz radar during energetic particle precipitation events in the summer of 2019. They used the sudden enhancements in electron densities derived from the VHF observations above 90 km as indicators of particle precipitation. They found that the altitude extent of the PMSE increased along with an enhancement of the strength of the pre-existing PMSE. On some occasions, PMSE suddenly appeared during particle precipitation events. After the particle precipitation subsided, the PMSE intensities continued to be stronger for a few minutes and then decreased. At the altitudes where the maximum enhancement in PMSE backscatter occurred, they found no corresponding broadening in the spectral widths. Interestingly, the most intense PMSE echoes almost always coincided with the lower values of spectral widths both during particle precipitations and other times. In some cases, the spectral widths showed well separated regimes between the upper and lower parts of the PMSE layers and this happened irrespective of particle precipitation. The frequency Doppler shifts showed alternating upward and downward motions without much difference before and after the particle precipitation. Based on these observations, Narayanan et al. (2022) conclude that the sudden enhancement in the electron densities during particle precipitation intensifies PMSE structures that match the Bragg scale of the incident radio wave thereby enabling an enhancement in the backscatter strength. Similarly, PMSE backscattering may get initiated in the altitudes in which the structures were already present but where electron density was not sufficient before the onset of precipitation. Spectral widths and Doppler velocities did not show sudden variations with particle precipitation because they depend on the neutral dynamics.

PMSE observations

Observations by Digisonde and VHF at EISCAT show that the irregular Es layers, called PMSE-Es (Polar Mesosphere Summer Echoes-Es), have some relationship with PMSE. H. Li et al. (2021) observed that the trends in the occurrence rates of PMSE-Es are similar to those of PMSE, although there are some notable differences. The occurrence rate of PMSE-Es is much lower than that of PMSE. The minimum value of PMSE-Es appears 1 h to 2 h earlier than that of PMSE, and PMSE-Es appears earlier than PMSE in the year.

The PMSE measured at different elevation angles from 78° to 90° at EISCAT VHF was examined (Figure 32). Ge, Li, Xu et al. (2021) found that the PMSE peak power and the strongest PMSE average power occur at the same elevation

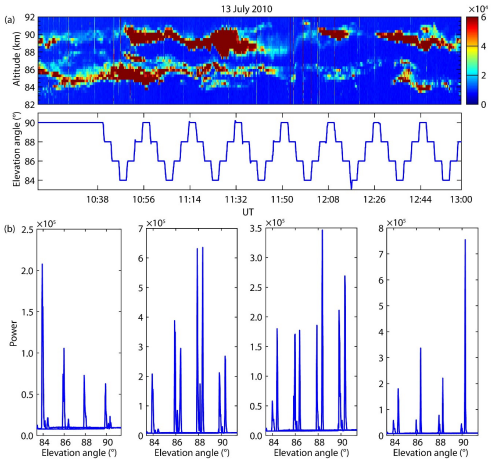

Figure 32: PMSE observations by the EISCAT VHF radar from 10:38UT to 13:00 UT on 13 July 2010. The scale of the PMSE intensity (as measured by power spectral density) is arbitrary. (a) Height-time contour plot for PMSE backscatter power spectral density in arbitrary unit (upper panel), and the corresponding elevation angles observing the PMSEs (bottom panel). (b) Median PMSE power intensity versus elevation angles during the four measurement cycles.

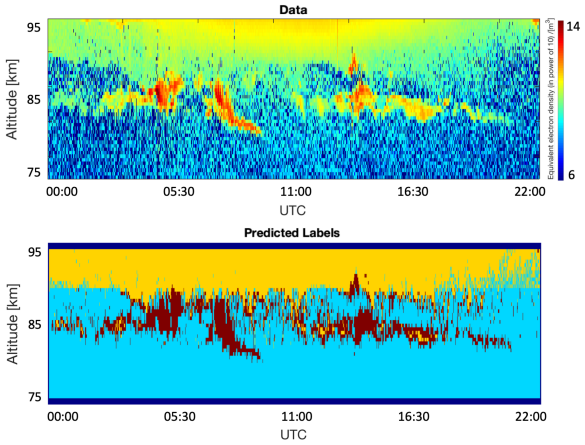

Figure 33: Results of segmentation using the random forests method ($mtry = 5$) and weighted-down labels technique from a study by Almeida et al. (2021). The data are obtained from the observation day, 7 July 2010. The image on the top illustrates the original image where the color scale represents the equivalent electron density to the power of 10, per cubic meter. The image at the bottom represents the predicted labels. Yellow, cyan and dark red represent, respectively, the region of the image labeled as Ionospheric background, Background noise, and PMSE. The horizontal axis on both images represents the time which starts at 00:00 UTC and finishes at 22:00 UTC. The vertical axis represents the altitude which ranges from 75 km to 95 km.

angles, and that the strongest PMSE occur at off-vertical angles when the PMSE has a layered (multilayer) structure. Additional investigations by Ge, Li, Xu et al. (2021) of the aspect sensitivity and the volume reflectivity of PMSE showed that the distribution curve, of the volume reflectivity occurrence rate at different elevation angles, obeys a Gaussian distribution as a whole, although there are some differences at different elevation angles. Additionally, the aspect sensitivity of the lower PMSE layer was found to be stronger than that of the upper PMSE layer, indicating that the lower PMSE layers are associated with more anisotropic turbulence scattering.

Segmentation of PMSE data using random forests

Jozwicki et al. (2022) presented an approach to segment Polar Mesospheric Summer Echoes (PMSE) from datasets obtained from EISCAT VHF radar data by manually labelling the data into three different categories: PMSE, Ionospheric background, and Background noise. For segmentation, they employed random forests on a set of simple features, including altitude derivative, time derivative, mean, median, standard deviation, minimum, and maximum values corresponding to neighborhood sizes ranging from 3 by 3 to 11 by 11 pixels. Next, in order to reduce the model bias and variance, they employed a method that decreases the weight applied to pixel labels with large uncertainty. The results indicated that it is possible to segment PMSE from the data using random forests (Figure 33), and that the weighted-down labels technique improves the performance of the random forests method.

Sounding rocket project "PMWE" for investigation of polar mesosphere winter echoes

A first sounding rocket campaign dedicated to investigate the creation mechanism of Polar Mesosphere Winter Echoes (PMWE) was conducted in April 2018 from the north Norwegian Andøya Space Center (69° N, 16° E). Two instrumented sounding rockets were launched on 13 and 18 April under PMWE and non-PMWE conditions, respectively. Strelnikov et al. (2021) give an overview of the PMWE sounding rocket

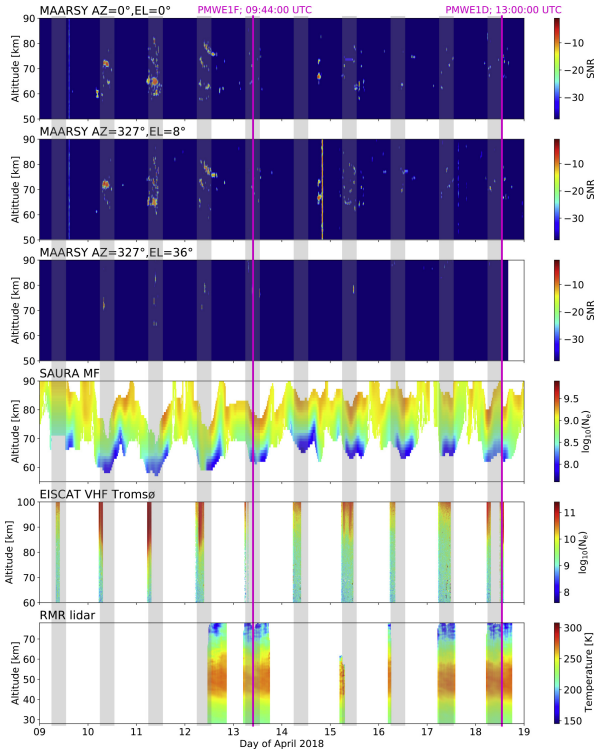

Figure 34: Launch conditions during the PMWE-1 rocket campaign. From top to bottom: Upper three panels show PMWE display observed by MAARSY's vertical, upleg, and downleg beams; The 4th panel shows smoothed electron density observed by the Saura partial reflection radar; The 5th panel shows EISCAT electron density measurements; The lower panel shows temperature measurements by the RMR lidar. Grey shading shows launch windows for every day and the magenta lines mark rocket launch times

mission. They describe and discuss some results of combined in situ and ground-based measurements which allow to verify existing PMWE theories (Figure 34). Their measurements ultimately show that: a) polar winter mesosphere is abounded with meteor smoke particles (MSP) and intermittent turbulent layers, b) all PMWE observed during this campaign can be explained by neutral air turbulence, c) turbulence creates small-scale structures in all D-region constituents, including free electrons; d) MSP ultimately influence the radar volume reflectivity by distorting the turbulence spectrum of electrons, e) the influence of MSP and of background electron density is just to increase SNR.

Effects of energetic particle precipitation on PMSE echoes observed by EISCAT UHF radar: A case study

The correlation between simultaneously occurring energetic particle precipitation and polar mesosphere summer echoes (PMSE) was studied by Rauf et al. (2022). The results showed that both positive and negative correlations were observed, and that energetic precipitating particles was one important, but not an essential, candidate for generating PMSE echoes.

Space plasma studies

Charged dust in the D-region incoherent scatter spectrum

Gunnarsdottir and Mann (2021) investigated the influence of charged dust (meteoric smoke particles, MSP) on the incoherent scatter spectrum in the ionospheric D-region. The dust particles are a result of meteor ablation, which generally occurs at altitudes from around 75 km to 120 km. The ablated material recondenses to form larger MSPs and are of the order of nanometres in size. These are then transported through the mesosphere-stratosphere system where they can influence chemical processes and the growth of ice particles. Current atmospheric models struggle to incorporate the effect of such particles as, due to their size and high altitude, they are very difficult to measure. The authors have developed a model to investigate how the dust size, density and charge state effects the shape of the ISR spectrum allowing the possibility for these parameters to be measured.

The model ISR spectrum uses typical ionospheric conditions (based on the IRI and NRLMISR-00 models) above Tromsø and the radar parameters of the EISCAT VHF radar. The inclusion of MSPs causes the ISR ion line spectrum to become larger in amplitude and the width to decrease when compared to a "normal" ISR spectrum (from an ionospheric plasma without MSPs). The authors note that whilst the backscatter cross section (ISR amplitude) does not change with the polarity of the dust, the width of the spectrum is affected. Figure 35 indicates the variation in both the spectrum amplitude and width as a function of dust size for two different bulk densities of dust. The plot on the left hand side shows the effect of negative dust whilst the right hand side plot shows the effect of positive dust. They

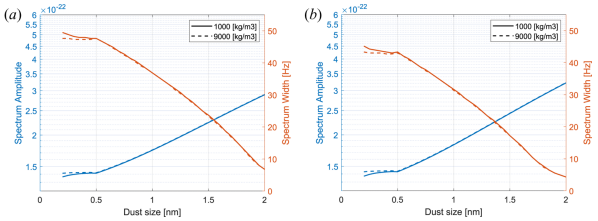

Figure 35: The variation in the spectrum amplitude (blue) and width (orange) for two different bulk densities of dust: 1000 kg m^{-3} (solid line) and 9000 kg m^{-3} (dashed line) for the case of (a) negatively charged dust and (b) positively charged dust. Dust number density was kept at 500 cm^{-3} and electron density at 5000 cm^{-3} whilst positive ion density was varied to maintain charge neutrality.

attribute this to the fact that positively charged dust particles effect the negative ion population more than negatively charged dust, resulting in a narrowing of the spectrum. The authors also find that, due to prevailing atmospheric conditions, dust detection is easier in the winter mesosphere than the summer mesosphere. The authors also note that although the spectrum is influenced by the presence of MSPs, as discussed above, it is often difficult to separate the effects of the MSPs from other ionospheric effects such as electron and neutral density and temperature changes. The authors suggest combining the ISR data with another independent data source for the ionospheric parameters would be a step towards isolating the MSP effects on the ISR spectrum.

Auroral-enhanced plasma lines by suprathermal electrons

Plasma line (PL) observed by EISCAT in the recent solar maximum 2014 were investigated by Feng et al. (2021). To statistically analyze the PL, an algorithm was developed to automatically extract the naturally enhanced PL from the ISR spectra (Figure 36), with which two typical auroral-enhanced PLs, secondary electron and electron beam, are analyzed. The result showed that PL originating from secondary electrons and electron beams present an evident magnetic local time dependence.

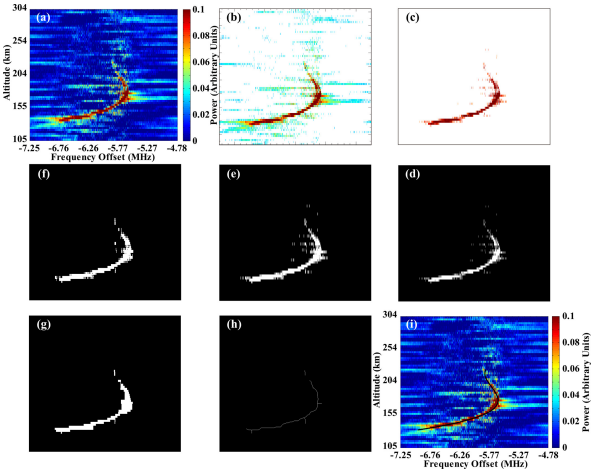

Figure 36: Panel(a)is a plasma line (PL) intensity profile obtained by the EISCAT ISR with altitude from 105 km to 304 km (mainly the E region and valley region) at 17:01UT on November 21, 2014. Enhanced PLs are extracted through morphological image processing in panels (b) to (h), which comprise preprocessing, color extraction, image binarization, morphological dilation, connectivity labeling, morphological erosion, and morphological thinning, respectively. Panel (i) presents the enhanced PLs extracted from the intensity profile in panel (a).

Publications 2021–2022

Akhmetov, O. I., Belakhovsky, V. B., Mingalev, I. V., Mingalev, O. V., Larchenko, A. V., & Suvorova, Z. V. (2022). About the propagation of RSDN-20 "Alpha" signals in the Earth-ionosphere waveguide during geomagnetic disturbances. *Radio Science*, *58*(1), e2022RS007490. https://doi.org/10.1029/2022rs007490

Akhmetov, O. I., Mingalev, I. V., Mingalev, O. V., Belakhovsky, V. B., & Suvorova, Z. V. (2021). Propagation of electromagnetic waves in the region of high latitudes at various states of the ionosphere at the frequencies of the RSDN-20 (Alpha) radionavigation system. *Geomagnetism and Aeronomy*, *61*(3), 376–388. https://doi.org/10.1134/s0016793221030026

Alfonsi, L., Bergeot, N., Cilliers, P. J., Franceschi, G. D., Baddeley, L., Correia, E., Mauro, D. D., Enell, C.-F., Engebretson, M., Ghoddousi-Fard, R., Häggström, I., Ham, Y.-b., Heygster, G., Jee, G., Kero, A., Kosch, M., Kwon, H.-J., Lee, C., Lotz, S., … Zou, S. (2022). Review of environmental monitoring by means of radio waves in the polar regions: From atmosphere to geospace. *Surveys in Geophysics*, *43*(6), 1609–1698. https://doi.org/10.1007/s10712-022-09734-z

Bakhmetieva, N. V., & Grigoriev, G. I. (2022). Study of the mesosphere and lower thermosphere by the method of creating artificial periodic irregularities of the ionospheric plasma. *Atmosphere*, *13*(9), 1346. https://doi.org/10.3390/atmos13091346

Belakhovsky, V. B., Jin, Y., & Miloch, W. (2022). Dayside scintillations of GPS signals according to the observations on the Svalbard archipelago. *Bulletin of the Russian Academy of Sciences: Physics*, *86*(3), 348–353. https://doi.org/10.3103/s1062873822030066

Belakhovsky, V. B., Jin, Y., & Miloch, W. J. (2021). Influence of different types of ionospheric disturbances on GPS signals at polar latitudes. *Annales Geophysicae*, *39*(4), 687–700. https://doi.org/10.5194/angeo-39-687-2021

Bender, S., Espy, P. J., & Paxton, L. J. (2021). Validation of SSUSI-derived auroral electron densities: Comparisons to EISCAT data. *Annales Geophysicae*, *39*(5), 899–910. https://doi.org/10.5194/angeo-39-899-2021

Birch, M., & Hargreaves, J. (2021). The dynamics of quasi-periodic ripples in the high-latitude F-region. *Journal of Atmospheric and Solar-Terrestrial Physics*, *216*, 105536. https://doi.org/10.1016/j.jastp.2021.105536

Bjoland, L. M., Ogawa, Y., Løvhaug, U. P., Lorentzen, D. A., Hatch, S. M., & Oksavik, K. (2021). Electron density depletion region observed in the polar cap ionosphere. *Journal of Geophysical Research: Space Physics*, *126*(1), e2020JA028432. https://doi.org/10.1029/2020ja028432

Blagoveshchenskaya, N., Borisova, T., Kalishin, A., Egorov, I., Yeoman, T., & Haggstrom, I. (2022). Simultaneous action of X- and O-mode HF pump waves on the high-latitude upper (F-region) ionosphere at EISCAT. *Universe*, *8*(2), 91. https://doi.org/10.3390/universe8020091

Bosse, L., Lilensten, J., Johnsen, M. G., Gillet, N., Rochat, S., Delboulbé, A., Curaba, S., Ogawa, Y., Derverchère, P., & Vauclair, S. (2022). The polarisation of auroral emissions: A tracer of the E region ionospheric currents. *Journal of Space Weather and Space Climate*, *12*, 17. https://doi.org/10.1051/swsc/2022014

Brask, S. M., Marholm, S., Mare, F. D., Adhikari, S., Spicher, A., Takahashi, T., & Miloch, W. J. (2022). Electron-neutral collisions effects on Langmuir probe in the lower E-region ionosphere. *Physics of Plasmas*, *29*(3), 033511. https://doi.org/10.1063/5.0079761

Cai, L., Aikio, A., Kullen, A., Deng, Y., Zhang, Y., Zhang, S.-R., Virtanen, I., & Vanhamäki, H. (2022). GeospaceLAB: Python package for managing and visualizing data in space physics. *Frontiers in Astronomy and Space Sciences*, *9*, 1023163. https://doi.org/10.3389/fspas.2022.1023163

Chen, J., Yang, J., Li, Q., Yan, Y., Hao, S., Wang, C., Wu, J., Xu, B., Xu, T., Che, H., & He, L. (2022). ELF/VLF wave radiation experiment by modulated ionospheric heating based on multi-source observations at EISCAT. *Atmosphere*, *13*(2), 228. https://doi.org/10.3390/atmos13020228

Collinson, G., Glocer, A., Pfaff, R., Barjatya, A., Bissett, S., Blix, K., Breneman, A., Clemmons, J., Eparvier, F., Gass, T., Michell, R., Mitchell, D., Imber, S., Ghalib, A., Akbari, H., Ansted, G., Baddeley, L., Bahr, H., Bain, G., … Wilson, T. (2022). The Endurance rocket mission. *Space Science Reviews*, *218*(5), 39. https://doi.org/10.1007/s11214-022-00908-0

Dalin, P., Suzuki, H., Pertsev, N., Perminov, V., Efremov, D., Voelger, P., Narayanan, V., Mann, I., Häggström, I., Zalcik, M., Ugolnikov, O., Hedin, J., Gumbel, J., Latteck, R., & Baumgarten, G. (2022). Studies of noctilucent clouds from the stratosphere during the SONC balloon-borne experiment in 2021. *Journal of Atmospheric and Solar-Terrestrial Physics*, *240*, 105959. https://doi.org/10.1016/j.jastp.2022.105959

Davydov, V. E., Zinkina, M. D., Pisanko, Y. V., Tertyshnikov, A. V., & Yurik, R. Y. (2021). Satellite observations of effects of auroral ionosphere heating with the EISCAT facility. *Russian Meteorology and Hydrology*, *46*(4), 241–244. https://doi.org/10.3103/s106837392104004x

Dreyer, J., Partamies, N., Whiter, D., Ellingsen, P. G., Baddeley, L., & Buchert, S. C. (2021). Characteristics of fragmented aurora-like emissions (FAEs) observed on Svalbard. *Annales Geophysicae*, *39*(2), 277–288. https://doi.org/10.5194/angeo-39-277-2021

Eliasson, B., Senior, A., Rietveld, M., Phelps, A. D. R., Cairns, R. A., Ronald, K., Speirs, D. C., Trines, R. M. G. M., McCrea, I., Bamford, R., Mendonça, J. T., & Bingham, R. (2021). Controlled beat-wave Brillouin scattering in the ionosphere. *Nature Communications*, *12*(1), 6209. https://doi.org/10.1038/s41467-021-26305-9

Enengl, F., Partamies, N., Ivchenko, N., & Baddeley, L. (2021). On the relationship of energetic particle precipitation and mesopause temperature. *Annales Geophysicae*, *39*(5), 795–809. https://doi.org/10.5194/angeo-39-795-2021

Fear, R. C. (2022). Joint Cluster/Ground-Based studies in the first 20 years of the Cluster mission. *Journal of Geophysical Research: Space Physics*, *127*(8), e2021JA029928. https://doi.org/10.1029/2021ja029928

Feng, T., Liu, M., Xu, B., Xu, T., Gao, S., Wang, X., & Zhou, C. (2021). Auroral-enhanced plasma lines by suprathermal electrons observed by EISCAT. *Journal of Geophysical Research: Space Physics*, *126*(3), e2020JA028495. https://doi.org/10.1029/2020ja028495

Frøystein, I. (2022, June). *Frequency dependence of ionospheric electron heating around the third double resonance* [MSc Thesis]. UiT the Arctic University of Norway. https://hdl.handle.net/10037/25830

Fu, H. Y., Jiang, M. L., Vierinen, J., Häggström, I., Rietveld, M. T., Varberg, E., Sato, H., Wu, J., Scales, W. A., & Jin, Y. Q. (2022). A stimulated emission diagnostic technique for electron temperature of the high power radio wave modified ionosphere. *Geophysical Research Letters*, *49*(15), e2022GL099390. https://doi.org/10.1029/2022gl099390

Fukizawa, M., Sakanoi, T., Ogawa, Y., Tsuda, T. T., & Hosokawa, K. (2021). Statistical study of electron density enhancements in the ionospheric F region associated with pulsating auroras. *Journal of Geophysical Research: Space Physics*, *126*(12), e2021JA029601. https://doi.org/10.1029/2021ja029601

Fukizawa, M., Sakanoi, T., Tanaka, Y., Ogawa, Y., Hosokawa, K., Gustavsson, B., Kauristie, K., Kozlovsky, A., Raita, T., Brändström, U., & Sergienko, T. (2022). Reconstruction of precipitating electrons and three-dimensional structure of a pulsating auroral patch from monochromatic auroral images obtained from multiple observation points. *Annales Geophysicae*, *40*(4), 475–484. https://doi.org/10.5194/angeo-40-475-2022

Ge, S., Li, H., Xu, B., Xu, T., Meng, L., Wang, M., Hannachi, A., Zhu, M., Broman, L., Ullah, S., & Rauf, A. (2021). Characteristic analysis of layered PMSEs measured with different elevation angles at VHF based on an experimental case. *Earth and Planetary Physics*, *5*(1), 1–10. https://doi.org/10.26464/epp2021001

Ge, S., Li, H., Xu, T., Xu, B., Meng, L., Zhu, M., Wang, M., Ullah, S., & Rauf, A. (2021). Aspect sensitivity of double-layer polar mesosphere summer echoes at VHF based on an experimental case. *Journal of Atmospheric and Solar-Terrestrial Physics*, *223*, 105741. https://doi.org/10.1016/j.jastp.2021.105741

Giono, G., Ivchenko, N., Sergienko, T., & Brändström, U. (2021). Multi-point measurements of the plasma properties inside an aurora from the SPIDER sounding rocket. *Journal of Geophysical Research: Space Physics*, *126*(7), e2021JA029204. https://doi.org/10.1029/2021ja029204

Gunnarsdottir, T. L., & Mann, I. (2021). Charged dust in the D-region incoherent scatter spectrum. *Journal of Plasma Physics*, *87*(5), 905870502. https://doi.org/10.1017/s0022377821000866

Günzkofer, F., Pokhotelov, D., Stober, G., Liu, H., Liu, H.-L., Mitchell, N. J., Tjulin, A., & Borries, C. (2022). Determining the origin of tidal oscillations in the ionospheric transition region with EISCAT radar and global simulation data. *Journal of Geophysical Research: Space Physics*, *127*(10), e2022JA030861. https://doi.org/10.1029/2022ja030861

Guo, Z., Fang, H., & Honary, F. (2021). A novel method to identify the physical mechanism and source region of ELF/VLF waves generated by beat-wave modulation using preheating technique. *Universe*, *7*(2), 43. https://doi.org/10.3390/universe7020043

Habarulema, J. B., Okoh, D., Burešová, D., Rabiu, B., Tshisaphungo, M., Kosch, M., Häggström, I., Erickson, P. J., & Milla, M. A. (2021). A global 3-D electron density reconstruction model based on radio occultation data and neural networks. *Journal of Atmospheric and Solar-Terrestrial Physics*, *221*, 105702. https://doi.org/10.1016/j.jastp.2021.105702

He, L., Chen, J., Lu, J., Yan, Y., Yang, J., Yuan, G., Hao, S., & Li, Q. (2022). A hybrid MPI/OpenMP parallelization scheme based on nested FDTD for parametric decay instability. *Atmosphere*, *13*(3), 472. https://doi.org/10.3390/atmos13030472

John, H. M., Forte, B., Astin, I., Allbrook, T., Arnold, A., Vani, B. C., Häggström, I., & Sato, H. (2021). An EISCAT UHF/ESR experiment that explains how ionospheric irregularities induce GPS phase fluctuations at auroral and polar latitudes. *Radio Science*, *56*(9), e2020RS007236. https://doi.org/10.1029/2020rs007236

John, H. M., Forte, B., Astin, I., Allbrook, T., Arnold, A., Vani, B. C., & Häggström, I. (2021). Performance of GPS positioning in the presence of irregularities in the auroral and polar ionospheres during EISCAT UHF/ESR measurements. *Remote Sensing*, *13*(23), 4798. https://doi.org/10.3390/rs13234798

Jozwicki, D., Sharma, P., & Mann, I. (2021). Investigation of polar mesospheric summer echoes using linear discriminant analysis. *Remote Sensing*, *13*(3), 522. https://doi.org/10.3390/rs13030522

Jozwicki, D., Sharma, P., Mann, I., & Hoppe, U.-P. (2022). Segmentation of PMSE data using random forests. *Remote Sensing*, *14*(13), 2976. https://doi.org/10.3390/rs14132976

Kalishin, A. S., Blagoveshchenskaya, N. F., Borisova, T. D., & Rogov, D. D. (2021). Remote diagnostics of effects induced by high-latitude heating facilities. *Russian Meteorology and Hydrology*, *46*(4), 231–240. https://doi.org/10.3103/s1068373921040038

Kalishin, A. S., Blagoveshchenskaya, N. F., Borisova, T. D., & Yeoman, T. K. (2021). Ion gyro-harmonic structures in stimulated emission excited by X-mode high power HF radio waves at EISCAT. *Journal of Geophysical Research: Space Physics*, *126*(8), e2020JA028989. https://doi.org/10.1029/2020ja028989

Kallio, E., Kero, A., Harri, A.-M., Kestilä, A., Aikio, A., Fontell, M., Jarvinen, R., Kauristie, K., Knuuttila, O., Koskimaa, P., Loyala, J., Lukkari, J.-M., Modabberian, A., Niittyniemi, J., Rynö, J., Vanhamäki, H., & Varberg, E. (2022). Radar—CubeSat transionospheric HF propagation observations: Suomi 100 satellite and EISCAT HF facility. *Radio Science*, *57*(10), e2022RS007516. https://doi.org/10.1029/2022rs007516

Kastinen, D. (2022, November). *From meteors to space safety: Dynamical models and radar measurements of space objects* [PhD Thesis]. Umeå University / Swedish Institute of Space Physics. http://urn.kb.se/resolve?urn=urn:nbn:se:umu:diva-200702

Kastinen, D., Tveito, T., Vierinen, J., & Granvik, M. (2020). Radar observability of near-Earth objects using EISCAT 3D. *Annales Geophysicae*, *38*(4), 861–879. https://doi.org/10.5194/angeo-38-861-2020

Kavanagh, A. J., Ogawa, Y., & Woodfield, E. E. (2022). Two techniques for determining F-region ion velocities at meso-scales: Differences and impacts on Joule heating. *Journal of Geophysical Research: Space Physics*, *127*(6), e2021JA030062. https://doi.org/10.1029/2021ja030062

Kebede, F. T. (2021, June). *Energetic electron precipitation of pulsating aurorae and their mesospheric effects* [PhD Thesis]. University of Bergen. https://hdl.handle.net/11250/2758892

Krasnov, V., Kuleshov, Y., Koristin, A., & Drobzheva, Y. (2022). Influence of the geomagnetic field on absorption of radiowaves. *Journal of Atmospheric and Solar-Terrestrial Physics*, *227*, 105806. https://doi.org/10.1016/j.jastp.2021.105806

Larchenko, A. V., Lebed', O. M., Blagoveshchenskaya, N. F., Pil'gaev, S., Beketova, E. B., & Fedorenko, Y. (2022). Features of the ELF/VLF wave generation and propagation processes during ionospheric modulated high-frequency heating. *Radiophysics and Quantum Electronics*, *64*(11), 761–779. https://doi.org/10.1007/s11141-022-10177-0

Li, H., Ge, S., Meng, L., Wang, M., Rauf, A., & Ullah, S. (2021). Exploring the occurrence rate of PMSE-Es by Digisonde at Tromsø. *Earth and Planetary Physics*, *5*(2), 187–195. https://doi.org/10.26464/epp2021017

Li, Z., Fang, H., Gong, H., & Guo, Z. (2021). Analysis of observations near the fourth electron gyrofrequency heating experiment in EISCAT. *Universe*, *7*(6), 191. https://doi.org/10.3390/universe7060191

Li, Z., Li, Q., Fang, H., & Gong, H. (2021). The apparent behavior of electron density during an alternating O/X-mode heating experiment. *Universe*, *7*(8), 274. https://doi.org/10.3390/universe7080274

Liu, J., Wang, W., Qian, L., Lotko, W., Burns, A. G., Pham, K., Lu, G., Solomon, S. C., Liu, L., Wan, W., Anderson, B. J., Coster, A., & Wilder, F. (2021). Solar flare effects in the Earth's magnetosphere. *Nature Physics*, *17*(7), 807–812. https://doi.org/10.1038/s41567-021-01203-5

Lu, H., Yang, J., Li, Q., Hao, S., Guo, F., Wu, J., Chen, J., Ma, G., & Xu, T. (2021). ELF/VLF communication experiment by modulated heating of ionospheric auroral electrojet at EISCAT. *IEEE Transactions on Antennas and Propagation*, *69*(4), 2267–2273. https://doi.org/10.1109/tap.2020.3026872

Mahmoudian, A., Kosch, M. J., Scales, W. A., Rietveld, M. T., & Pinedo, H. (2022). Neutral air turbulence in the mesosphere and associated polar mesospheric summer echoes (PMSEs). *Radio Science*, *57*(2), e2021RS007371. https://doi.org/10.1029/2021rs007371

McKay, D., Grydeland, T., & Gustavsson, B. (2022). Manx arrays: Perfect non-redundant interferometric geometries. *Radio Science*, *57*(9), e2022RS007500. https://doi.org/10.1029/2022rs007500

Miyoshi, Y., Hosokawa, K., Kurita, S., Oyama, S.-I., Ogawa, Y., Saito, S., Shinohara, I., Kero, A., Turunen, E., Verronen, P. T., Kasahara, S., Yokota, S., Mitani, T., Takashima, T., Higashio, N., Kasahara, Y., Matsuda, S., Tsuchiya, F., Kumamoto, A., … Nakamura, S. (2021). Penetration of MeV electrons into the mesosphere accompanying pulsating aurorae. *Scientific Reports*, *11*(1), 13724. https://doi.org/10.1038/s41598-021-92611-3

Moser, C., LaBelle, J., Hatch, S., Moen, J. I., Spicher, A., Takahashi, T., Kletzing, C. A., Bounds, S., Oksavik, K., Sigernes, F., & Yeoman, T. K. (2021). The cusp as a VLF saucer source: First rocket observations of long-duration VLF saucers on the dayside. *Geophysical Research Letters*, *48*(2), e2020GL090747. https://doi.org/10.1029/2020gl090747

Nanjo, S., Nozawa, S., Yamamoto, M., Kawabata, T., Johnsen, M. G., Tsuda, T. T., & Hosokawa, K. (2022). An automated auroral detection system using deep learning: Real-time operation in Tromsø, Norway. *Scientific Reports*, *12*(1), 8038. https://doi.org/10.1038/s41598-022-11686-8

Narayanan, V. L., Häggström, I., & Mann, I. (2022). Effects of particle precipitation on the polar mesospheric summer echoes observed by EISCAT VHF 224 MHz radar. *Advances in Space Research*, *69*(9), 3350–3361. https://doi.org/10.1016/j.asr.2022.02.015

Nel, A. E., Kosch, M. J., Whiter, D., Gustavsson, B., & Aslaksen, T. (2021). A new auroral phenomenon, the anti-black aurora. *Scientific Reports*, *11*(1), 1829. https://doi.org/10.1038/s41598-021-81363-9

Nikolaeva, V., Gordeev, E., Nikolaev, A., Rogov, D., & Troshichev, O. (2022). Auroral ionosphere model with PC index as an input. *Atmosphere*, *13*(3), 402. https://doi.org/10.3390/atmos13030402

Oyama, S.-i., Vanhamäki, H., Cai, L., Aikio, A., Rietveld, M., Ogawa, Y., Raita, T., Kellinsalmi, M., Kauristie, K., Kozelov, B., Shinbori, A., Shiokawa, K., Tsuda, T. T., & Sakanoi, T. (2022). Ther-

mospheric wind response to a sudden ionospheric variation in the trough: Event at a pseudo-breakup during geomagnetically quiet conditions. *Earth, Planets and Space*, *74*(1), 154. https://doi.org/10.1186/s40623-022-01710-6

Pakhotin, I. P., Burchill, J. K., Förster, M., & Lomidze, L. (2022). The Swarm Langmuir probe ion drift, density and effective mass (SLIDEM) product. *Earth, Planets and Space*, *74*(1), 109. https://doi.org/10.1186/s40623-022-01668-5

Partamies, N., Tesema, F., & Bland, E. (2022). Appearance and precipitation characteristics of high-latitude pulsating aurora. *Frontiers in Astronomy and Space Sciences*, *9*, 923396. https://doi.org/10.3389/fspas.2022.923396

Rauf, A., Li, H. L., Ullah, S., Meng, L., Wang, B., & Ge, S. C. (2022). Effects of energetic particle precipitation on PMSE echoes observed by EISCAT UHF radar: A case study. *Geomagnetism and Aeronomy*, *62*(4), 495–504. https://doi.org/10.1134/s0016793222040028

Rexer, T. (2021, November). *Radio wave propagation through the ionosphere* [PhD Thesis]. UiT the Arctic University of Norway. https://hdl.handle.net/10037/22976

Rexer, T., Leyser, T., Gustavsson, B., & Rietveld, M. (2021). Conditions for topside ion line enhancements. *Journal of Geophysical Research: Space Physics*, *126*(7), e2021JA029379. https://doi.org/10.1029/2021ja029379

Rietveld, M. T., & Stubbe, P. (2022). History of the Tromsø ionosphere heating facility. *History of Geo- and Space Sciences*, *13*(1), 71–82. https://doi.org/10.5194/hgss-13-71-2022

Ross, S., Arjas, A., Virtanen, I. I., Sillanpää, M. J., Roininen, L., & Hauptmann, A. (2022). Hierarchical deconvolution for incoherent scatter radar data. *Atmospheric Measurement Techniques*, *15*(12), 3843–3857. https://doi.org/10.5194/amt-15-3843-2022

Sailer, G. (2021). *The polar silk road*. Kehrer Verlag. https://www.kehrerverlag.com/en/gregor-sailer-the-polar-silk-road-978-3-96900-045-8

Sato, H., Rietveld, M. T., & Jakowski, N. (2021). GLONASS observation of artificial field-aligned plasma irregularities near magnetic zenith during EISCAT HF experiment. *Geophysical Research Letters*, *48*(4), e2020GL091673. https://doi.org/10.1029/2020gl091673

Schult, C., Kero, J., Stober, G., & Brown, P. (2021). Dual frequency measurements of meteor head echoes simultaneously detected with the MAARSY and EISCAT radar systems. *Icarus*, *355*, 114137. https://doi.org/10.1016/j.icarus.2020.114137

Sivokon', V., & Cherneva, N. (2022). Dynamic characteristics of field-aligned ionospheric irregularities under the conditions of ionosphere modification. In *Springer proceedings in Earth and environmental sciences* (pp. 473–479). Springer International Publishing. https://doi.org/10.1007/978-3-030-91467-7_35

Stamm, J. (2022, May). *Advanced signal processing techniques with eiscat3d* [PhD Thesis]. UiT the Arctic University of Norway. https://hdl.handle.net/10037/25066

Stamm, J., Vierinen, J., & Gustavsson, B. (2021). Observing electric field and neutral wind with EISCAT 3D. *Annales Geophysicae*, *39*(6), 961–974. https://doi.org/10.5194/angeo-39-961-2021

Stamm, J., Vierinen, J., Urco, J. M., Gustavsson, B., & Chau, J. L. (2021). Radar imaging with EISCAT 3D. *Annales Geophysicae*, *39*(1), 119–134. https://doi.org/10.5194/angeo-39-119-2021

Stepanov, N. A., Sergeev, V. A., Shukhtina, M. A., Ogawa, Y., Chu, X., & Rogov, D. D. (2021). Ionospheric electron density and conductance changes in the auroral zone during substorms. *Journal of Geophysical Research: Space Physics*, *126*(7), e2021JA029572. https://doi.org/10.1029/2021ja029572

Strelnikov, B., Staszak, T., Latteck, R., Renkwitz, T., Strelnikova, I., Lübken, F.-J., Baumgarten, G., Fiedler, J., Chau, J. L., Stude, J., Rapp, M., Friedrich, M., Gumbel, J., Hedin, J., Belova, E., Hörschgen-Eggers, M., Giono, G., Hörner, I., Löhle, S., … Fasoulas, S. (2021). Sounding rocket project "PMWE" for investigation of polar mesosphere winter echoes. *Journal of Atmospheric and Solar-Terrestrial Physics*, *218*, 105596. https://doi.org/10.1016/j.jastp.2021.105596

Takada, M., Seki, K., Ogawa, Y., Keika, K., Kasahara, S., Yokota, S., Hori, T., Asamura, K., Miyoshi, Y., & Shinohara, I. (2021). Low-altitude ion upflow observed by EISCAT and its effects on supply of molecular ions in the ring current detected by Arase (ERG). *Journal of Geophysical Research: Space Physics*, *126*(5), e2020JA028951. https://doi.org/10.1029/2020ja028951

Tarnecki, L. K., Marshall, R. A., Stober, G., & Kero, J. (2021). Meteoroid mass estimation based on single-frequency radar cross section measurements. *Journal of Geophysical Research: Space Physics*, *126*(9), e2021JA029525. https://doi.org/10.1029/2021ja029525

Tesema, F., Partamies, N., Whiter, D. K., & Ogawa, Y. (2022). Types of pulsating aurora: Comparison of model and EISCAT electron density observations. *Annales Geophysicae*, *40*(1), 1–10. https://doi.org/10.5194/angeo-40-1-2022

Tesfaw, H. W., Virtanen, I. I., Aikio, A. T., Nel, A., Kosch, M., & Ogawa, Y. (2022). Precipitating electron energy spectra and auroral power estimation by incoherent scatter radar with high temporal resolution. *Journal of Geophysical Research: Space Physics*, *127*(4), e2021JA029880. https://doi.org/10.1029/2021ja029880

Tveito, T., Vierinen, J., Gustavsson, B., & Narayanan, V. L. (2021). Planetary radar science case for EISCAT 3D. *Annales Geophysicae*, *39*(3), 427–438. https://doi.org/10.5194/angeo-39-427-2021

Ullah, S., Li, H., Rauf, A., Meng, L., Wang, B., Wang, M., & Ge, S. (2021). Comparison of modulated UHF PMSE characteristics at different altitude ranges. *Advances in Space Research*, *68*(1), 236–245. https://doi.org/10.1016/j.asr.2021.03.015

Virtanen, I. I., Tesfaw, H. W., Roininen, L., Lasanen, S., & Aikio, A. (2021). Bayesian filtering in incoherent scatter plasma parameter fits. *Journal of Geophysical Research: Space Physics*, *126*(3), e2020JA028700. https://doi.org/10.1029/2020ja028700

Wannberg, G. (2022). History of EISCAT - Part 5: Operation and development of the system during the first 2 decades. *History of Geo- and Space Sciences*, *13*(1), 1–21. https://doi.org/10.5194/hgss-13-1-2022

Whiter, D. K., Sundberg, H., Lanchester, B. S., Dreyer, J., Partamies, N., Ivchenko, N., Fraia, M. Z. D., Oliver, R., Serpell-Stevens, A., Shaw-Diaz, T., & Braunersreuther, T. (2021). Fine-scale dynamics of fragmented aurora-like emissions. *Annales Geophysicae*, *39*(6), 975–989. https://doi.org/10.5194/angeo-39-975-2021

Wu, J., Blagoveshchenskaya, N., Wu, J., Shen, X., Rietveld, M. T., Haggstrom, I., Xu, T., & Xu, Z. (2021). Altitude descents in high-frequency enhanced plasma and ion lines during ionospheric heating at EISCAT. *Journal of Atmospheric and Solar-Terrestrial Physics*, *212*, 105425. https://doi.org/10.1016/j.jastp.2020.105425

Wu, J., Wu, J., Haggstrom, I., Xu, T., Xu, Z., & Hu, Y. (2022). Incoherent scatter radar observation of high frequency enhanced ion and plasma lines by X/O mode pump around critical altitude. *Earth and Planetary Physics*, *6*(4), 1–8. https://doi.org/10.26464/epp2022038

Xiong, J., Yuan, K., Tang, R., Yao, M., Deng, X., Zhao, Z., Chen, H., & Haggstrom, I. (2022). An improved iterative algorithm utilized in data processing for incoherent scatter radar. *IEEE Geoscience and Remote Sensing Letters*, *19*, 1–5. https://doi.org/10.1109/lgrs.2021.3109087

Yamauchi, M., Keyser, J. D., Parks, G., Oyama, S.-i., Wurz, P., Abe, T., Beth, A., Daglis, I. A., Dandouras, I., Dunlop, M., Henri, P., Ivchenko, N., Kallio, E., Kucharek, H., Liu, Y. C.-M., Mann, I., Marghitu, O., Nicolaou, G., Rong, Z., … Yoshikawa, I. (2022). Plasma-neutral gas interactions in various space environments: Assessment beyond simplified approximations as a Voyage 2050 theme. *Experimental Astronomy*, *54*(2-3), 521–559. https://doi.org/10.1007/s10686-022-09846-9

Yang, J., Li, Q., Lu, H., Hao, S., Chen, J., Yan, Y., Wu, J., & Xu, T. (2022). Experimental ELF/VLF wave communication with excitation by ionosphere modulated heating. *Radio Science*, *57*(3), e2021RS007406. https://doi.org/10.1029/2021rs007406

EISCAT Operations 2021–2022

The EISCAT radars operate in two basic modes, using approximately half the available observing time for each. In the Special Programme mode, users conduct individual experiments dedicated to specific experiments and objectives. The resulting data are reserved for the exclusive use of the experimenters for one year from the date of collection. Special programmes often make use of the well developed pulse schemes and observing modes of the Common Programme. EISCAT Common Programmes are conducted for the benefit of the entire user community and the resulting data are immediately available to all.

More than one of the EISCAT radars are often operated simultaneously during the Common Programme experiments. Such observations offer comprehensive data sets for atmospheric, ionospheric, and magnetospheric studies.

Common Programme One, CP-1, uses a fixed transmitting antenna, pointing along the geomagnetic field direction. The three-dimensional velocity and the anisotropy in other parameters can be measured using the VHF receiving stations at Kiruna and Sodankylä. CP-1 is capable of providing results with very good time resolution and is suitable for studies of substorm phenomena, particularly auroral processes where conditions might change rapidly. Continuous electric field measurements can be derived from the tri-static F-region data. On longer time scales, CP-1 measurements support studies of diurnal changes, such as atmospheric tides, as well as seasonal and solar-cycle variations.

Common Programme Two, CP-2, is designed to make measurements from a small, rapid transmitter antenna scan. One aim is to identify wave-like phenomena with length and time scales comparable with, or larger than, the scan (a few tens of kilometers and about ten minutes). The first three positions form a triangle with vertical, south, and south-east positions, while the fourth is aligned with the geomagnetic field.

Common Programme Three, CP-3, covers a 10° latitudinal range in the F-region with a 17-position scan up to 74°N in a 30 min cycle. The observations are made in a plane defined by the magnetic meridian through Tromsø. The principal aim of CP-3 is the mapping of ionospheric and electrodynamic parameters over a broad latitude range.

Common Programme Four, CP-4, covers geographic latitudes up to almost 80°N (77°N invariant latitude) using a low elevation, split-beam configuration. CP-4 is particularly suitable for studies of high latitude plasma convection and polar cap phenomena. However, with the present one-beam configuration of the VHF radar, CP-4 is run with either both UHF and VHF radars or with UHF only in a two position scan.

Common Programme Six, CP-6, is designed for low altitude studies, providing spectral measurements at mesospheric heights. The velocity and electron density are derived from the measurements, and the spectra contain information on the aeronomy of the mesosphere. A vertical antenna pointing direction is used.

Common Programme Seven, CP-7, probes high altitudes and is particularly aimed at polar wind studies. The present version, with only one of the VHF klystrons running, is designed to cover altitudes up to 1500 km vertically above Ramfjordmoen.

Equivalent Common Programme modes are available for the EISCAT Svalbard Radar: CP-1 is directed along the geomagnetic field (81.6° inclination). CP-2 uses a four position scan where the 32 m antenna moves between three of the posisitions, and data is collected by the 42 m antenna while the other one is moving. CP-3 is a 15 position elevation scan using the 32 m antenna with southerly beam swinging positions. CP-4 combines observations in the F-region viewing area with field-aligned and vertical measurements. CP-6 is similar to the mainland radar CP-6. CP-7 is similar to the mainland radar CP-7.

The tables on the next four pages summarise the accounted hours on the various facilities for each month and for each Common Programme mode (CP) or Associate (SP) for the years 2021 and 2022.

KST COMMON PROGRAMMES

2021	Jan	Feb	Mar	Apr	May	Jun	Jul	Aug	Sept	Oct	Nov	Dec	Total	%	Target%
CP1	42.5		15	1.5					38		1		98	26	16
CP2	107.5					56							163.5	43	16
CP3			24						1				25	7	12
CP4				2.5									2.5	1	10
CP6				3	70			1			14.5		88.5	23	20
CP7				1									1	0	18
UP													0	0	
Total	150	0	39	8	70	56	0	1	39	0	15.5	0	**378.5**	100	
%	40	0	10	2	18	15	0	0	10	0	4	0	100		

KST SPECIAL PROGRAMMES

2021	Jan	Feb	Mar	Apr	May	Jun	Jul	Aug	Sept	Oct	Nov	Dec	Total	Incl AA	Move	Target
CN													0	5		44
FI			8.5					4	8		87		107.5	121		118
NI			12									60	72	80		69
NO			8.5	24		33.5		35	4	30	7	11	153	175		193
SW			8.5					35	4	92.5	32		172	202		258
UK						24		32		24	32		112	133		183
AA	19.5	24	16	8					10.5	14		8	100			
Total	19.5	24	53.5	32	0	57.5	0	106	26.5	160.5	158	79	**716.5**	**717**	**0**	**864**
%	3	3	7	4	0	8	0	15	4	22	22	11	100			

	EI	CN	FI	NI	NO	SW	UK	
Target		5.06	13.71	7.95	22.29	29.86	21.13	%

KST OTHER PROGRAMMES

2021	Jan	Feb	Mar	Apr	May	Jun	Jul	Aug	Sept	Oct	Nov	Dec	Total	Target
PP										51	31		82	104
EI													0	28
GE									9.5			7	16.5	30
FR													0	7
UA													0	5
KR													0	0
US													0	5
TB													0	0
Total	0	0	0	0	0	0	0	0	9.5	51	31	7	**98.5**	**179**

KST TOTALS

2021	Jan	Feb	Mar	Apr	May	Jun	Jul	Aug	Sept	Oct	Nov	Dec	Total	Target
CP	150	0	39	8	70	56	0	1	39	0	15.5	0	378.5	504
SP	19.5	24	53.5	32	0	57.5	0	106	26.5	160.5	158	79	716.5	864
OP	0	0	0	0	0	0	0	0	9.5	51	31	7	98.5	179
Total	169.5	24	92.5	40	70	113.5	0	107	75	211.5	204.5	86	**1193.5**	**1547**

USAGE BREAKDOWN

2021	Jan	Feb	Mar	Apr	May	Jun	Jul	Aug	Sept	Oct	Nov	Dec	Total	Target
UHF	169.5	24	87	35		56		29	65.5	76	156.5	75	773.5	696
VHF			4	5	53.5	48		46	8	112.5	46	6.5	329.5	696
ESR	184	0	76.5	0	51.5	78	0	10.5	50.5	45.5	153.5	94.5	744.5	948
Heating								15		32	3	5	55	155
Total Radar	353.5	24	167.5	40	105	182	0	100.5	124	266	359	181	1949	2495
Passive KST			8		82	48		86	8			1	233	
Passive ESR													0	

ESR COMMON PROGRAMMES

2021	Jan	Feb	Mar	Apr	May	Jun	Jul	Aug	Sept	Oct	Nov	Dec	Total	%	Target%
CP1	148		38						33.5	5	25.5	3	253	68	54
CP2						54		1.5					55.5	15	16
CP3									5				5	1	12
CP4													0	0	10
CP6					51.5						6		57.5	15	
CP7												1	1	0	
UP													0	0	
Total	148	0	38	0	51.5	54	0	1.5	38.5	5	31.5	4	**372**	100	
%	40	0	10	0	14	15	0	0	10	1	8	1	100		

ESR SPECIAL PROGRAMMES

2021	Jan	Feb	Mar	Apr	May	Jun	Jul	Aug	Sept	Oct	Nov	Dec	Total	Incl AA	Move	Target
CN													0	0	0	24
FI			5					3	4	5.5	40		57.5	58	0	64
NI	4		11.5								8.5	19	43	43	0	37
NO	32		17					3	4	5.5	6	19.5	87	87	0	104
SW			5					3	4	5.5	49	1.5	68	68	0	139
UK						24				24	14.5	43.5	106	106	0	98
AA													0			
Total	36	0	38.5	0	0	24	0	9	12	40.5	118	83.5	**361.5**	**362**	**0**	**466**
%	10	0	11	0	0	7	0	2	3	11	33	23	100			

ESR OTHER PROGRAMMES

2021	Jan	Feb	Mar	Apr	May	Jun	Jul	Aug	Sept	Oct	Nov	Dec	Total	Target
PP											4		4	32
EI													0	22
GE												7	7	0
FR													0	0
UA													0	0
KR													0	32
TB													0	0
Total	0	0	0	0	0	0	0	0	0	0	4	7	**11**	**86**

ESR TOTALS

2021	Jan	Feb	Mar	Apr	May	Jun	Jul	Aug	Sept	Oct	Nov	Dec	Total	Target
CP	148	0	38	0	51.5	54	0	1.5	38.5	5	31.5	4	372	396
SP	36	0	38.5	0	0	24	0	9	12	40.5	118	83.5	361.5	466
OP	0	0	0	0	0	0	0	0	0	0	4	7	11	86
Total	184	0	76.5	0	51.5	78	0	10.5	50.5	45.5	153.5	94.5	**744.5**	**948**

KST COMMON PROGRAMMES

2022	Jan	Feb	Mar	Apr	May	Jun	Jul	Aug	Sept	Oct	Nov	Dec	Total	%	Target %
CP1			80	13	0.5				1.5				95	25	16
CP2	135					104							239	62	16
CP3													0	0	12
CP4				1	0.5								1.5	0	10
CP6			11	1.5									12.5	3	20
CP7									39				39	10	18
UP													0	0	
Total	135	0	91	15.5	1	104	0	0	40.5	0	0	0	**387**	100	
%	35	0	24	4	0	27	0	0	10	0	0	0	100		

KST SPECIAL PROGRAMMES

2022	Jan	Feb	Mar	Apr	May	Jun	Jul	Aug	Sept	Oct	Nov	Dec	Total	Incl AA	Move	Target
CN		28				11.5					5	14	58.5	62		55
FI	20.5										34	38.5	93	104		108
NI	14.5	19	39								12	16.5	101	109		80
NO		17.5	36.5	26	18	2.5		46.5			8	20.5	175.5	203		271
SW		11	4.5	0.5				46.5		6		116	184.5	211		259
UK					13.5						33	34	80.5	96		150
AA	12	16	16						8	20	19.5		91.5			
Total	47	91.5	96	26.5	31.5	14	0	93	8	26	111.5	239.5	**784.5**	**785**	**0**	**905**
%	6	12	12	3	4	2	0	12	1	3	14	31	100			

	EI	CN	FI	NI	NO	SW	UK	
Target		4	11.98	8.83	29.92	28.66	16.61	%

KST OTHER PROGRAMMES

2022	Jan	Feb	Mar	Apr	May	Jun	Jul	Aug	Sept	Oct	Nov	Dec	Total	Target
PP		6.5								5.5	22	2.5	36.5	65
EI													0	28
GE									8	11			19	27
FR													0	0
UA													0	5
KR												121	121	0
US													0	13
TB			9.5								8		17.5	18
Total	0	6.5	9.5	0	0	0	0	0	8	16.5	30	123.5	**194**	**156**

KST TOTALS

2022	Jan	Feb	Mar	Apr	May	Jun	Jul	Aug	Sept	Oct	Nov	Dec	Total	Target
CP	135	0	91	15.5	1	104	0	0	40.5	0	0	0	387	504
SP	47	91.5	96	26.5	31.5	14	0	93	8	26	111.5	239.5	784.5	905
OP	0	6.5	9.5	0	0	0	0	0	8	16.5	30	123.5	194	156
Total	182	98	196.5	42	32.5	118	0	93	56.5	42.5	141.5	363	**1365.5**	**1564**

USAGE BREAKDOWN

2022	Jan	Feb	Mar	Apr	May	Jun	Jul	Aug	Sept	Oct	Nov	Dec	Total	Target
UHF	153	73.5	145.5	41.5	1	110			10.5	34	119	208	896	732
VHF	29	6.5	41.5		31	2		66.5	52	5	17.5	132.5	383.5	732
ESR	161.5	1	129.5	36	15.5	94	0	0	19	27.5	95	58	637	961
Heating		19.5	6.5			5.5				3.5	5	9	49	100
Total Radar	343.5	100.5	323	77.5	47.5	211.5	0	66.5	81.5	70	236.5	407.5	2018	2525
Passive KST			13		3	2		133	10			102.5	263.5	
Passive ESR													0	

ESR COMMON PROGRAMMES

2022	Jan	Feb	Mar	Apr	May	Jun	Jul	Aug	Sept	Oct	Nov	Dec	Total	%	Target %
CP1	133	1	83	12.5	0.5	53			19		9		311	82	54
CP2													0	0	16
CP3													0	0	12
CP4													0	0	10
CP6						41							41	11	
CP7										27.5	1		28.5	7	
UP													0	0	
Total	133	1	83	12.5	0.5	94	0	0	19	27.5	10	0	**380.5**	100	
%	35	0	22	3	0	25	0	0	5	7	3	0	100		

ESR SPECIAL PROGRAMMES

2022	Jan	Feb	Mar	Apr	May	Jun	Jul	Aug	Sept	Oct	Nov	Dec	Total	Incl AA	Move	Target
CN													0	0	0	0
FI											38	22	60	60	0	58
NI			22										22	22	0	43
NO	12.5		24.5		7.5						10	24	78.5	79	0	146
SW				23.5									23.5	24	0	140
UK	16				7.5						37	12	72.5	73	0	81
AA													0			
Total	28.5	0	46.5	23.5	15	0	0	0	0	0	85	58	**256.5**	**257**	**0**	**487**
%	11	0	18	9	6	0	0	0	0	0	33	23	100			

ESR OTHER PROGRAMMES

2022	Jan	Feb	Mar	Apr	May	Jun	Jul	Aug	Sept	Oct	Nov	Dec	Total	Target
PP													0	0
EI													0	22
GE													0	0
FR													0	0
UA													0	0
KR													0	56
TB													0	0
Total	0	0	0	0	0	0	0	0	0	0	0	0	**0**	**78**

ESR TOTALS

2022	Jan	Feb	Mar	Apr	May	Jun	Jul	Aug	Sept	Oct	Nov	Dec	Total	Target
CP	133	1	83	12.5	0.5	94	0	0	19	27.5	10	0	380.5	396
SP	28.5	0	46.5	23.5	15	0	0	0	0	0	85	58	256.5	487
OP	0	0	0	0	0	0	0	0	0	0	0	0	0	78
Total	161.5	1	129.5	36	15.5	94	0	0	19	27.5	95	58	**637**	**961**

EISCAT organisational diagram, December 2022.

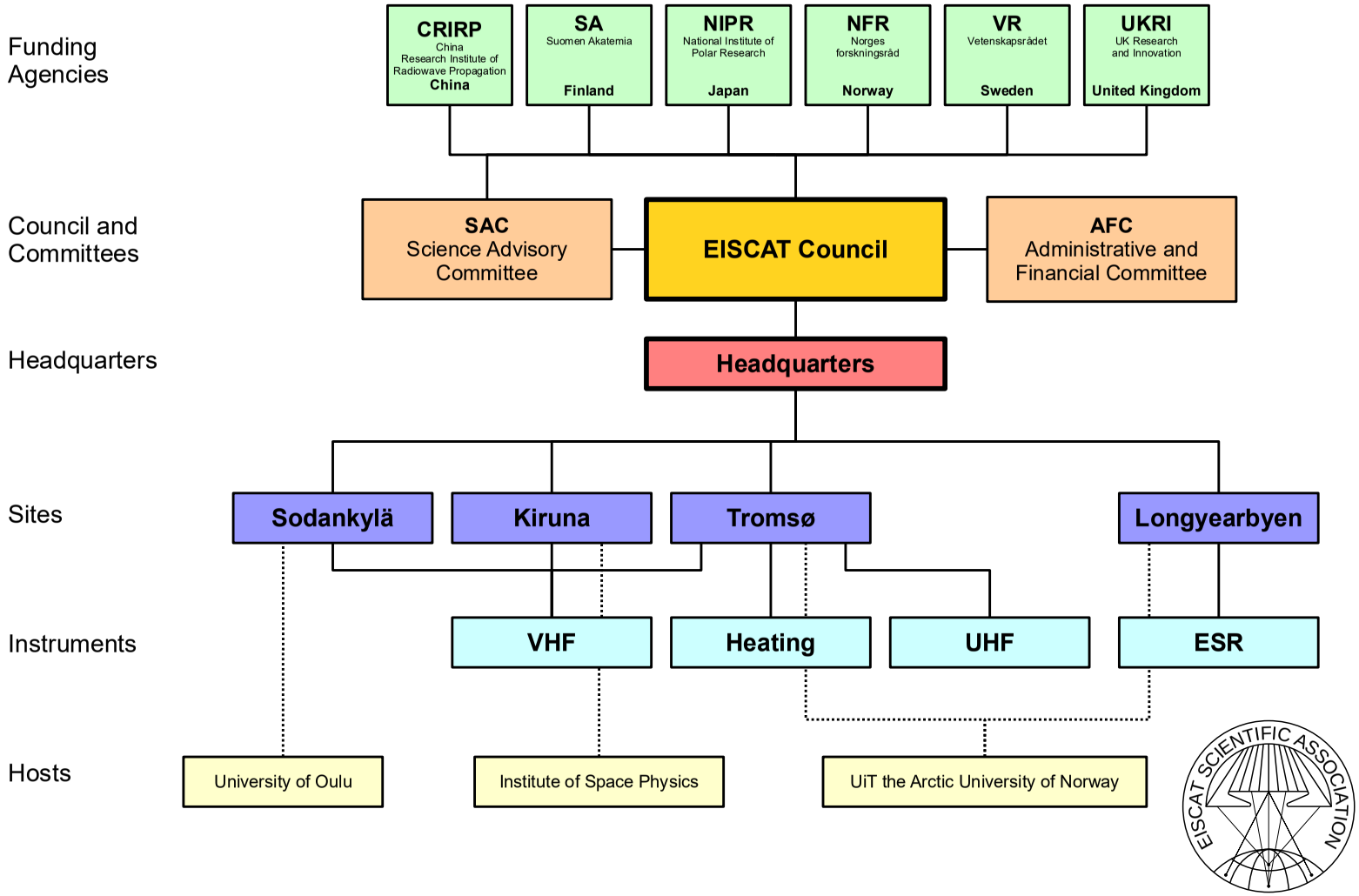

Photo from the Annual Review Meeting, 5–7 December 2022, at Welcome Inn Hotel Lyngskroa in Oteren, Norway. From left: Erik Varberg, Harri Hellgren, Assar Westman, Robert Juhlin, Emma Unander, Elisabet Goth, Simon Brown, Mária Miháliková, Trond Sandmo, Stian Grande, Magnus Thorebäck, Arild Stenberg, Erlend Danielsen, Anders Tjulin, Espen Helgesen, Taishi Hashimoto, Axel Steuwer, Juri Katkalov, Jussi Markkanen, Esa Wikström, Craig Heinselman, David Rutberg, Carl-Fredrik Enell, Johan Svensson, Henrik Andersson.

EISCAT Scientific Association

December 2022

EISCAT Director

Dr. C. Heinselman

EISCAT Council

P. R. of China	
Dr. Z. Ding	
Prof. J. Wu	Delegate
Finland	
Prof. A. Aikio	*Chair*
Dr. K. Sulonen	Delegate
Prof. P. Verronen	
Japan	
Prof. H. Miyaoka	Delegate
Dr. S. Nozawa	
Norway	
Prof. P. Espy	
Prof. I. Mann	
Dr. P. Sørgaard	Delegate
Sweden	
Dr. T. Andersson	Delegate
Prof. J. Gumbel	*Vice-Chair*
Dr. O. Norberg	
United Kingdom	
Prof. M. Freeman	Delegate
Prof. I. W. McCrea	

Administrative and Finance Committee (AFC)

Dr. R. Chaplin	United Kingdom
Dr. M. Friberg	Sweden
Prof. H. Miyaoka	Japan
Dr. I. Solheim	*Chair*, Norway
Ms. M. Vannas	Finland

Scientific Advisory Committee (SAC)

Prof. L. Baddeley	Norway
Dr. J. Berdermann	Germany (affiliate)
Dr. S. Buchert	Sweden
Dr. G. Jee	S. Korea (affiliate)
Dr. A. Kavanagh	United Kingdom
Dr. Y.-S. Kwak	S. Korea (affiliate)
Dr. R. Latteck	External member
Dr. Y. Ogawa	*Chair*, Japan
Dr. T. Ulich	Finland
Dr. D. Vakoch	United States (affiliate)
Dr. R. Varney	External member
Dr. A. Vartanyan	United States (affiliate)
Prof. J. Wu	P. R. of China
Dr. A. Zalizovski	Ukraine (affiliate)

Senior Management

Mr. H. Andersson	Head of Adm., Deputy Dir.
Dr. C. Heinselman	Director

Site Leaders

Mr. E. Helgesen	EISCAT Svalbard Radar
Mr. J. Markkanen	Sodankylä Site
Mr. A. Stenberg	Tromsø Site
Mr. M. Thorebäck	Kiruna Site

Appendix:

EISCAT Scientific Association Annual Report, 2021

EISCAT Scientific Association
Registered as a Swedish non-profit organisation
Organisation number: 897300-2549

Annual financial report for the year 2021-01-01 – 2021-12-31

The EISCAT Council and the Director for the Association submits herewith the annual report for 2021.

ADMINISTRATION REPORT

Ownership, organisation and objective

The EISCAT Scientific Association was established in 1975 through an agreement between six European organisations. Japan joined in 1996 and the People's Republic of China in 2007.

The EISCAT Associates at 2021-12-31 are: China Research Institute of Radiowave Propagation (People's Republic of China), National Institute of Polar Research (Japan), Norges forskningsråd (Norway), Suomen Akatemia (Finland), UK Research and Innovation (United Kingdom of Great Britain and Northern Ireland) and Vetenskapsrådet (Sweden).

The now-running EISCAT Agreement came into force 2017-06-20, with all Associates making long term funding commitments to the Association. The Association has its formal seat in Kiruna, Sweden, and is registered as a non-profit organisation.

The aim of the Association is to make significant progress in the understanding of physical processes in geospace, in the high latitude atmosphere, and in the coupling between the high and low latitudes and altitudes. For this purpose, the Association has developed, constructed, and now operates, a number of radar facilities at high latitudes. At present, these comprise a system of stations at Tromsø (Norway), Kiruna (Sweden), Sodankylä (Finland), and Longyearbyen (Svalbard). The new system, EISCAT_3D, is currently being constructed.

The Association is fully funded by the Associates, but additional operations may also be funded by short term additional contributions from both Associate and non-Associate bodies. Depending on the available funding, scientific priorities and operational targets are adjusted on an annual basis.

The EISCAT Council is charged with the overall administration and supervision of the Association's activities. The Council appoints a Director, who is responsible for the daily management and operation of the facilities of the Association.

Operation and scientific development

The EISCAT Radars systems operated reliably throughout the year and 1 938 hours were accounted in 2021 (1 918 hours in 2020).

Common Programmes amounted to 39% (49%) of the operations. Special Programmes amounted to 56% (44%) and other operations amounted to 5% (7%) of the total hours.

DLR-SO (Germany), IRA-NASU (Ukraine), JHUAPL (USA), KASI (South Korea), KOPRI (South Korea) and METI (Int.) have Affiliate agreements and totally 24 hours (52 hours) were accounted to the affiliates. METI joined and CNRS-IRAP (France) left the Association during 2021. The Peer-Review Programme made it possible for user groups from P. R of China, Finland, Germany, Japan and Russia to run experiments, at no cost, on the systems. Peer-Review time amounted to 86 accounted hours (72 hours).

Future operation and scientific development
The current EISCAT systems are ready for users. These include the EISCAT Svalbard Radar, Heating and the UHF and VHF radars with the possibility to run the VHF in tristatic mode by using the antennas in Kiruna and Sodankylä for reception.

The new EISCAT_3D radar system is being constructed. EISCAT_3D will replace the current UHF and VHF radar systems. The new system comprises three phased arrays working together. These will be built in Finland, Norway and Sweden. The construction of EISCAT_3D progress is slower than planned due to COVID-19 effects; components shortages and travel restrictions meaning that completion date will slip into 2023. The old UHF and VHF radar systems will be decommissioned after the new system has been taken in full use.

Project activities
The European Commission funded project EOSC-hub ended during the year. The two new Commission funded projects started, EGI-ACE and PITHIA-NRF, and ENVRI-FAIR continued throughout the year. Two other minor projects started too.

EISCAT_3D project
The ongoing EISCAT_3D Stage 1 (E3DS1) construction project continued throughout the year. All major industry contracts are in place and mass-production of the sub-systems have started. Deliveries of some parts are though on-hold due to electronic component shortages. The planned delivery and installation in 2021 of the antenna units from P. R. China could not be done due to COVID-19 travel restrictions. The Chinese contractor plan now to deliver the units in summer 2022. The electronics to be delivered by other contractors can hopefully be finalised late 2022.

A contract for the site buildings was agreed upon in the beginning of 2021 and both the Norwegian and Finnish sites now have buildings being constructed. The groundworks at the Swedish could not be completed in time before winter came in 2021. The work will be completed in 2022 and the buildings will thereafter be constructed.

The work of the Council and its committees
Due to COVID-19 all Council and Committee meetings were held digitally. Council met in spring and autumn and the meetings were chaired by the new Chairperson for 2021, Prof. Anita Aikio. In addition to regular matters, Council finalised the process of hiring the next Director to join in 2023. The new Director will be Dr. Axel Steuwer. He joins the Association in May 2022 starting as Director Designate. The present Director, Dr. Craig Heinselman, continues until the end of 2022.

The regular Council committees, the Administrative and Finance Committee (AFC) and the Scientific Advisory Committee (SAC) both had two digital meetings each during the year.

Budget development during the year
The 2021 operations ended below the budgeted target. This was much due to users travel restrictions. Likewise, the same restrictions meant almost no travel by EISCAT staff resulting in a cost reduction.

The budgeted income ended overall close to target, though Associate contributions were lower than planned. Further income from Affiliates and financial management plus a partial insurance coverage of the water leak from 2020 compensated.

In summary, the year ended in a small net profit.

The long-term budget plan

The long-term budget plan remains on a challenging but feasible level. The operating cost implications for the *new EISCAT*, with EISCAT_3D as the main system on the mainland, are well understood and with the doubling of the annual contribution from at least the Nordic countries, mean that the first years in the five-year plan can be balanced, though with less operations than optimal. Additional income via grants or other revenues will be needed to better utilise the new investments.

The result for 2021 and profit/loss handling

The year ended in a net profit of 25 kSEK, which will be added to the designated surplus fund for use in subsequent years.

PROFIT AND LOSS ACCOUNTS

in thousands of Swedish Crowns

	Note 1	*2021*	*2020*
Income from operations			
Grants received	Note 2	152 331	93 961
Revenue from operations	Note 3	0	0
Other income from operations	Note 4	460	81
		152 791	94 042
Expenses from operations			
Operation costs	Note 5	-6 448	-7 797
Administration costs		-17 314	-2 711
Personnel costs	Note 6	-26 671	-26 021
Depreciation of fixed assets		-8 677	-8 799
		-59 110	-45 328
Operating profit/loss		**93 681**	**48 714**
Financial items			
Interest income		16	203
Other financial income and cost		13 380	-7 520
		13 396	-7 317
Other items			
Income from sold inventory		35	2 462
Net profit/loss for the year		**107 113**	**43 859**

Changes in designated funds	Note 7	
Net profit/loss for the year	107 113	43 859
Use of designated investment funds	-74 091	-43 087
Use of other designated funds	-93	-216
Allocation of unused designated investment and other funds	-32 904	2 562
Net profit/loss for the year after redistributions	**25**	**3 118**

ANW

BALANCE SHEET

in thousands of Swedish Crowns

		2021	2020
ASSETS			
Fixed assets			
Tangible fixed assets	Note 8		
Buildings		74 115	55 223
Radar systems		204 742	149 536
Equipment and tools		2 109	2 115
		280 966	206 874
Current assets			
Receivables		1 969	37 479
Prepayments and accrued income	Note 9	3 008	3 179
Cash at bank and in hand	Note 10	328 314	313 546
		333 291	354 203
Total assets		**614 257**	**561 078**
CAPITAL AND LIABILITIES			
Capital			
Funds invested	Note 11	280 966	206 874
Designated funds	Note 12	69 376	44 682
Net income for the year after redistribution		25	3 118
		350 366	254 674
Current liabilities			
Accounts payable, trade		23 883	22 362
EISCAT_3D build grants received but not used	Note 13	231 882	279 303
External project grants received but not used	Note 14	6 224	3 777
Other liabilities		1 901	961
		263 891	306 404
Total capital and liabilities		**614 257**	**561 078**

STATEMENT OF CASH FLOWS

in thousands of Swedish Crowns

	2021	*2020*
Operating activities		
Operating result before financial items	93 681	48 714
Transfer from funds invested	8 677	8 799
Interest received	16	203
Financial income and cost	13 380	-7 520
Other income and cost	35	2 462
Increase/decrease of receivables	35 510	-28 894
Increase/decrease of prepayments and accrued income	171	-978
Increase/decrease of creditors and liabilities	-42 513	89 638
Adjustment for items not included in cash flow	-11 421	6 329
Cash flow from operations	**97 536**	**118 754**
Investment activities		
Investments in tangible assets	-82 768	-51 886
Cash flow from investment activities	**-82 768**	**-51 886**
Cash flow for the year	**14 767**	**66 868**
Liquid assets at the beginning of the year	**313 546**	**246 678**
Liquid assets at the end of the year	**328 314**	**313 546**

NOTES	2021	2020

Note 1 *Accounting principles*

The accounting and valuation principles applied are consistent with the provisions of the Swedish Annual Accounts Act and generally accepted accounting principles (for 2017 onwards, bokföringsnämnden allmänna råd och vägledningar, BFNAR 2012:1 K3).

All amounts are in thousands of Swedish kronor (SEK) unless otherwise stated.

Income

Received grants are reported as income in the period when they were claimed or received. Conditional grants are recognised as income when the associated conditions have been met. Income and revenue from operations, which include own-account funds, are reported as income when they were claimed or received. Grants and other income in foreign currencies have been accounted in the amounts estimated to be received, based on individual assessment.

Employee benefits

Ongoing remuneration to employees, either direct employed or provided via host agreements, in the form of salaries, social security, contributions to pension schemes and staff related insurances are accounted as personnel costs. Other remunerations, in cash, like travel subsistences or as benefits in-kind, like clothing, training and health care are also accounted as personnel costs. Overhead cost on host provided personnel is considered as external services accounted as administration cost.

Financial income

Dividends and interest income are accounted when credited the account.

Receivables

Receivables are stated at the amounts estimated to be received, based on individual assessment.

Receivables and payables in foreign currencies

Receivables and payables in foreign currencies are valued at the closing day rate. Where hedging measures have been used, such as forwarding contracts, the agreed exchange rate is applied. Gains and losses relating to operations are accounted for under other financial income and cost.

Bank accounts in foreign currencies

Bank balances in foreign currencies are valued at the closing day rate.

Fixed assets

Tangible fixed assets are stated at their original acquisition values after deduction of depreciation according to plan. Assets are depreciated systematically over their estimated useful lives. The following periods of depreciation are applied: Buildings 5 - 50 years, Radar systems 3 - 30 years and Equipment and tools 1 - 5 years.

Note 2 *Grants received*

The Associates contributed to the operation during the year in accordance with the EISCAT agreement and later additions. The Affiliates contributed according to agreed annual commitments. Income from European Commission (EC) funded projects were also accounted as received grants. The E3DS1 project started 2017-09-01 and the resulting projects costs were covered by the Associates (see Note 13) and other funds. Received project grants from the Associates are first accounted as prefinancing. Project costs are thereafter covered by withdrawals from prefinancing and at that time accounted as income from operations.

	2021	2020
Associates	33 764	24 328
Affiliates	1 891	904
Project grants, EC	3 114	2 401
Project grant, E3DS1	113 562	66 328
	152 331	93 961

Accumulated Associate contributions status as of 2021-12-31

Annual contributions included and for 2021, Finland, Japan (in cash and in-kind), Norway and Sweden were credited for providing E3DS1 project-related funds. These sums are used for EISCATs ownership and time-share calculation

Associate P. R. of China	53 337	49 434
Associate Finland	146 056	132 376
Associate Japan	117 118	100 595
Associate Norway	330 028	251 539
Associate Sweden	295 373	262 717
Associate UK	317 806	315 284
Previous Associates	382 168	382 168
	1 641 886	1 494 113

Note 3 *Revenue from operations*

The Association can, at rates related to the costs involved and as available, sell observation hours to Associates, Affiliates and other parties. Income from such selling of time are considered to be revenue. In 2021, no time-buyers used the systems.

Income from time-buyers	0	0

Note 4 *Other income from operations*

The Association supports visiting users by offering site accommodation and equipment hosting for either campaign brought instruments or for longer deployments. Educational support is done by providing teachers and/or other resources (like laboratory support). For 2021, the insurance company covered costs resulting from a water leak on Svalbard that happened in 2020.

Accommodation	4	44
Instrument hosting agreements	21	21
Educational support	18	16
Other income	416	-0
	460	81

Note 5 *Operations*

The annual operating target for all systems together is about 2 500 active (high power mode) hours. For 2021, the budget assumed 2 495 hours and the outcome became 1 903 hours. Passive hours come in addition. Such hours have a minimal effect on cost since the systems do not draw more electricity than in an off mode. Accounted hours are usually lower than the sum of operating hours since some systems have a charge rate that is less than 1-to-1.

Active hours (high-power), per system	*Hours*	*Hours*
EISCAT Svalbard Radar	745	700
UHF system	774	743
VHF system	330	330
Heating system	55	91
	1 903	1 863
Passive hours (receive only)		
Kiruna receiver system	117	134
Sodankylä receiver system	117	134
	233	268

	2021	2020
Accounted hours	*Hours*	*Hours*
Common programmes	751	946
Special programmes	1 078	848
Other hours	110	125
	1 938	1 918
Distribution of special programme hours between Associates		
Associate P. R. of China	0	0
Associate Finland	165	131
Associate Japan	115	132
Associate Norway	240	111
Associate Sweden	240	180
Associate UK	218	205
All Associates, AA-runs	100	91
	1 078	848
Distribution, other hours		
Affiliates	24	52
EISCAT staff and tests	0	0
Peer-reviewed campaigns	86	73
Timebuyers	0	0
	110	125

Note 6 *Personnel costs and average number of employees*

The Association employs directly Headquarters and most project staff, currently about 17 positions, including the Director. Of these, seven are on shorter-term project employments. The Headquarters is located in Kiruna, Sweden. The personnel working at the Kiruna (Sweden), Sodankylä (Finland), Svalbard and Tromsø (Norway) sites are normally not employed by the Association. Instead, the personnel are provided via site contracts by the Swedish Institute of Space Physics (Kiruna site staff but currently none), Oulu University (Sodankylä staff) and the Arctic University of Norway (Tromsø and Svalbard staff). The Association refunds all expenses related to the provided staff, as well as an additional overhead.

Personnel costs in total		
Salaries and emoluments paid to the Director	2 153	2 087
Other personnel, employed and provided via site contracts	16 539	15 915
Social security contributions amounted to	7 863	7 843
of which for pension costs	*3 748*	*3 943*
Other personnel costs	115	177

The Director, Dr. Craig Heinselman, started his employment 2013-01-01. His employment contract ends 2022-12-31. The next Director following after Dr. Heinselman has been recruited.

Of the pension costs, 373 kSEK (380 kSEK) relates to the Director. He and all other directly employed staff are included in ITP like occupational pension plans. For the personnel provided via site contracts, the pension plans are handled by their respective employer.

The members of the board (EISCAT Council) and members of committees, who represents Associates and Affiliates, do not receive remunerations from the Association. Travel expenses in connection with Council and committee meetings are normally covered by the Associates and Affiliates. The Association reimburses though the travel costs for Committee Chairpersons and external members.

	2021	2020
Salaries and emoluments and average number of staff per country		
Finland		
Salaries and emoluments	686	704
Average number of staff - men and women	1 + 0	1 + 0
Norway (including Svalbard)		
Salaries and emoluments	4 725	4 605
Average number of staff - men and women	7 + 0	8 + 0
Sweden		
Salaries and emoluments	13 281	12 693
Average number of staff - men and women	14 + 3	15 + 2

Members of the board and Directors at year-end - men and women

The board consist of delegations from every Associate country each having a Delegate (formal member) and up to two Representatives.

Board members (EISCAT Council)	11 + 3	10 + 4
Directors	1 + 0	1 + 0

Note 7 *Changes in designated funds*

Positive numbers - use of designated funds. Negative - transfer to the designated reserves or funds for later use.

Net profit/loss for the year	107 113	43 859
EISCAT_3D financial gains/losses taken in project finances	-11 420	6 329
Changes to capital operating reserve	-97	74
Changes to decommissioning fund	-2 623	-1 651
Changes to E3D construction reserve	-3 360	-2 116
Changes to five-year operating reserve	-15 500	0
Changes to funds invested	-74 091	-43 087
Changes to spare parts reserve	4	13
Changes to surplus fund	0	-303
	25	3 118

Note 8 *Tangible fixed assets*

Changes in tangible fixed assets.

Buildings		
Opening acquisition value	96 400	94 576
Acquisitions during the year	19 383	2 456
Disposals during the year	0	-632
Closing acquisition value	115 783	96 400
Opening accumulated depreciation	-41 177	-41 313
Depreciations during the year	-492	-495
Disposals during the year	0	632
Closing accumulated depreciation	-41 668	-41 177
Closing residual value	74 115	55 223
Radar systems		
Opening acquisition value	414 152	365 705
Acquisitions during the year	62 420	48 455
Disposals during the year	0	-8
Closing acquisition value	476 572	414 152
Opening accumulated depreciation	-264 616	-257 417
Depreciations during the year	-7 213	-7 206
Disposals during the year	0	8
Closing accumulated depreciation	-271 830	-264 616
Closing residual value	204 742	149 536

	2021	2020
Equipment and tools		
Opening acquisition value	36 306	36 345
Acquisitions during the year	965	975
Disposals during the year	-715	1 014
Closing acquisition value	36 557	36 306
Opening accumulated depreciation	-34 191	-34 087
Depreciations during the year	-972	-1 097
Disposals during the year	715	993
Closing accumulated depreciation	-34 448	-34 191
Closing residual value	2 109	2 115
Sum tangible fixed assets	280 966	206 874

Note 9 *Prepayments and accrued income*

Resources in staff and direct costs spent in ongoing externally funded projects are covered by accrued income until settled by submission of periodic report claims. In 2021, ENRVI-FAIR continued and four new projects started, whereof two, EGI-ACE and PITHIA-NRF, are EC funded. The EOSC-hub project ended 31 March 2021.

Prepaid rents	9	9
Prepaid insurances	852	789
Accrued income, previous projects	0	1 672
Accrued income, EGI-ACE project	459	0
Accrued income, ENVRI-FAIR project	0	638
Accrued income, PITHIA-NRF project	1 459	0
Accrued income, other projects	10	0
Other items	219	70
	3 008	3 179

Note 10 *Bank balances status*

Nordea	328 314	313 546
Cash in hand	0	0
	328 314	313 546

Note 11 *Funds invested status*

Buildings	74 115	55 223
Radar Systems	204 742	149 536
Equipment and Tools	2 109	2 115
	280 966	206 874

Note 12 *Designated funds*

The designated funds are divided into funds and reserves. The five-year operating reserve is new for 2021. It is used for budget transfers between periods in the five years plan. The other funds are earmarked for specific purposes.

Capital operating reserve	3 154	3 057
E3D construction reserve	11 786	8 425
Decommissioning fund	9 198	6 576
Equipment repair fund	754	754
Five-year operating reserve	15 500	0
Investment fund	7 753	7 753
Restructuring reserve	4 101	4 101
Spare parts reserve	80	84
Surplus fund	17 050	13 931
	69 376	44 682

	2021	2020

Note 13 *EISCAT_3D build grants received but not usea*

The construction project, E3DS1, started 2017-09-01 and its first phase, Stage 1, will be completed in 2022. Most Associates have now committed to its realisation. E3DS1 specific funding payments from Japan and Finland were received in 2021. Associate funds are kept as prefinancing until used in the project. Funds spent are deducted from the different funding sources in accordance with the agreed funding plan. United Kingdom contributed to the construction project during 2017-2018 and the funds were also used during that period. Sweden made an additional contribution in 2021 to cover for local taxes on costs in Sweden.

Changes in EISCAT_3D build grants received but not used

Associate Finland		
Opening balance	42 948	20 555
Received during the year	25 749	36 817
Used during the year	-6 131	-14 424
Closing balance	62 567	42 948
Associate Japan		
Opening balance	23 765	0
Received during the year	6 898	23 765
Used during the year	-14 297	0
Closing balance	16 367	23 765
Associate Norway		
Opening balance	176 580	121 470
Received during the year	0	78 398
Used during the year	-66 148	-23 288
Closing balance	110 432	176 580
Associate Sweden		
Opening balance	37 870	56 379
Received during the year	0	0
Used during the year	-26 986	-18 509
Closing balance	10 884	37 870
E3DS1 project finances, gains/losses		
Opening balance	-1 861	4 469
Changes during the year	11 420	-6 329
Closing balance	9 560	-1 861
Local taxes Sweden contribution		
Opening balance	0	0
Received during the year	26 000	0
Used during the year	-3 927	0
Closing balance	22 073	0
Sum EISCAT_3D received build grants	231 882	279 303

Note 14 *External project grants received but not usea*

Most externally funded projects work with prefinancing. For European Commission projects, these are in EUR's. The prefinancing is used to cover reported and approved costs. EOSC-hub was financially concluded during 2021.

EGI-ACE H2020 prefinancing	480	0
ENVRI-FAIR H2020 prefinancing	2 725	2 667
EOSC-hub prefinancing	0	1 110
PITHIA-NRF H2020 prefinancing	3 019	0
	6 224	3 777

Appendix:

EISCAT Scientific Association Annual Report, 2022

EISCAT Scientific Association
Registered as a Swedish non-profit organisation
Organisation number: 897300-2549

Annual financial report for the year 2022-01-01 – 2022-12-31

The EISCAT Council and the Director for the Association submits herewith the annual report for 2022.

ADMINISTRATION REPORT

Ownership, organisation and objective

The EISCAT Scientific Association was established in 1975 through an agreement between six European organisations. Japan joined in 1996 and the People's Republic of China in 2007.

The EISCAT Associates at 2022-12-31 are: China Research Institute of Radiowave Propagation (People's Republic of China), National Institute of Polar Research (Japan), Norges forskningsråd (Norway), Suomen Akatemia (Finland), UK Research and Innovation (United Kingdom of Great Britain and Northern Ireland) and Vetenskapsrådet (Sweden).

The now-running EISCAT Agreement came into force 2017-06-20, with all Associates making long term funding commitments to the Association. The Association has its formal seat in Kiruna, Sweden, and is registered as a non-profit organisation.

The aim of the Association is to make significant progress in the understanding of physical processes in geospace, in the high latitude atmosphere, and in the coupling between the high and low latitudes and altitudes. For this purpose, the Association has developed, constructed, and now operates, a number of radar facilities at high latitudes. At present, these comprise a system of stations at Tromsø (Norway), Kiruna (Sweden), Sodankylä (Finland), and Longyearbyen (Svalbard). The new system, EISCAT_3D, is currently being constructed.

The Association is fully funded by the Associates, but additional operations may also be funded by short term additional contributions from both Associate and non-Associate bodies. Depending on the available funding, scientific priorities and operational targets are adjusted on an annual basis.

The EISCAT Council is charged with the overall administration and supervision of the Association's activities. The Council appoints a Director, who is responsible for the daily management and operation of the facilities of the Association.

Operation and scientific development

The EISCAT Radars systems operated reliably throughout the year and 2 007 hours were accounted in 2022 (1 938 hours in 2021).

Common Programmes amounted to 38% (39%) of the operations. Special Programmes amounted to 52% (56%) and other operations amounted to 10% (5%) of the total hours.

Affiliates from Germany and South Korea made use of their access to the systems and totally 140 hours (24 hours) were accounted the affiliates. The Peer-Review Programme (PP) made it possible for user groups from Belgium and Germany to run experiments, at no cost, on the systems. In the beginning of the year, a Russian group ran a PP-campaign. Their access was thereafter cancelled. PP-time amounted to 36 accounted hours (86 hours). The new Transnational Access (TNA) project, PITHIA-NRF, funded two campaigns in 2022. Totally 18 hours (0 hours) were TNA-hours.

Future operation and scientific development
The current EISCAT systems are ready for users. These include the EISCAT Svalbard Radar, Heating and the UHF and VHF radars with the possibility to run the VHF in tristatic mode.

The new EISCAT_3D radar system is being constructed. EISCAT_3D will replace the current UHF and VHF radar systems. The new system comprises three phased arrays working together. These are currently built in Finland, Norway, and Sweden. The construction of EISCAT_3D suffers from delays due to earlier COVID-19 effects, components shortages and travel restrictions. It is expected that most of the hardware installations can be completed late 2023 followed by system commissioning and first regular full system operations in 2024. The old mainland UHF and VHF radar systems, which will be replaced by the new EISCAT_3D system, will be decommissioned latest at that time.

Project activities
In 2022, five externally funded projects are ongoing, whereof three are European Commission funded: EGI-ACE, ENVRI-FAIR and PITHIA-NRF.

EISCAT_3D project
The ongoing EISCAT_3D Stage 1 (E3DS1) construction project continued in fast pace throughout the year. The site buildings are almost ready for takeover and the site infrastructure are mostly completed. The antenna system delivered from P. R. China arrived harbour in Norway in September 2022 and was thereafter transported to the three EISCAT_3D sites. Installation of the units commenced thereafter. The installation works were tendered, and two companies were contracted for the work. The plan is to have the antenna installation fully completed latest summer 2023. Installation of the radar electronics will be done thereafter.

The work of the Council and its committees
The EISCAT Council had two regular meetings and an extraordinary one in 2022. The spring meeting was a hybrid meeting with most members present in Helsinki, Finland. That meeting had a follow-up hybrid session on Arlanda, Sweden, in September. The regular autumn meeting was also held as hybrid with most members present in Cambridge, UK. The meetings were chaired by Prof. Anita Aikio. In addition to regular matters, Council considered regulatory and legal matters relating to operating the new EISCAT_3D system. For that reason, Council formed a working group to assess this further. Members in the group are the delegates from the EISCAT_3D host countries, Finland, Norway, and Sweden. The findings and recommendations from the working group will be considered further during 2023. In the autumn meeting, Council thanked the outgoing Director, Dr. Craig Heinselman for his services to the Association over the last 10 years. The new Director, Dr. Axel Steuwer starts his term 2023-01-01. At the end of the year, Prof. Aikio handed over the Chairpersonship to Prof. Jörg Gumbel, who will be leading Council for the next two years, 2023 and 2024.

The regular Council committees, the Administrative and Finance Committee (AFC) and the Scientific Advisory Committee (SAC) both had two meetings each during the year. The spring meetings were on-line only and the autumn meetings were hybrid.

Budget development during the year
The 2022 operations ended below the budgeted target. Apart from operations, the Association has much recovered from COVID-19 effects and EISCAT scientists attended conferences and meetings much as before. The 20th International EISCAT Symposium was held in Eskilstuna, Sweden, in August and over 100 participants attending either physically or on-line.

The actual contributions from Associates and Affiliates became higher than budgeted due to changes in exchange rates. Less operations meant reduced costs, but electricity and staff expenses became higher due to costlier kWh costs and one-off costs. The overall operating costs ended much on target.

In summary, the year ended in a small net profit.

The long-term budget plan
The long-term budget plan remains on a challenging but feasible level, at least during the first years. Additional income via grants or other revenues will be needed to better utilise the new investments.

The result for 2022 and profit/loss handling
The year ended in a net profit of 501 kSEK, which will be added to the designated surplus fund for use in subsequent years.

PROFIT AND LOSS ACCOUNTS

in thousands of Swedish Crowns

	Note 1	*2022*	*2021*
Income from operations			
Grants received	Note 2	157 694	152 331
Revenue from operations	Note 3	0	0
Other income from operations	Note 4	83	460
		157 778	152 791
Expenses from operations			
Operation costs	Note 5	-17 541	-6 448
Administration costs		-3 002	-17 314
Personnel costs	Note 6	-29 581	-26 671
Depreciation of fixed assets		-8 720	-8 677
		-58 843	-59 110
Operating profit/loss		**98 935**	**93 681**
Financial items			
Interest income		1 442	16
Other financial income and cost		-1 695	13 380
		-253	13 396
Other items			
Income from sold inventory		37	35
Net profit/loss for the year		**98 718**	**107 113**

Changes in designated funds	Note 7		
Net profit/loss for the year		98 718	107 113
Use of designated investment funds		-75 099	-74 091
Use of other designated funds		-1 002	-93
Allocation of unused designated investment and other funds		-22 116	-32 904
Net profit/loss for the year after redistributions		**501**	**25**

BALANCE SHEET

in thousands of Swedish Crowns

		2022	*2021*
ASSETS			
Fixed assets			
Tangible fixed assets	Note 8		
Buildings		84 976	74 115
Radar systems		268 551	204 742
Equipment and tools		2 538	2 109
		356 065	280 966
Current assets			
Receivables		4 394	1 969
Prepayments and accrued income	Note 9	4 434	3 008
Cash at bank and in hand	Note 10	232 988	328 314
		241 816	333 291
Total assets		**597 881**	**614 257**
CAPITAL AND LIABILITIES			
Capital			
Funds invested	Note 11	356 065	280 966
Designated funds	Note 12	76 452	69 376
Net income for the year after redistribution		501	25
		433 018	350 366
Current liabilities			
Accounts payable, trade		33 682	23 883
EISCAT_3D build grants received but not used	Note 13	125 395	231 882
External project grants received but not used	Note 14	4 416	6 224
Other liabilities		1 371	1 901
		164 863	263 891
Total capital and liabilities		**597 881**	**614 257**

STATEMENT OF CASH FLOWS

in thousands of Swedish Crowns

	2022	*2021*
Operating activities		
Operating result before financial items	98 935	93 681
Transfer from funds invested	8 720	8 677
Interest received	1 442	16
Financial income and cost	-1 695	13 380
Other income and cost	37	35
Increase/decrease of receivables	-2 425	35 510
Increase/decrease of prepayments and accrued income	-1 425	171
Increase/decrease of creditors and liabilities	-99 028	-42 513
Adjustment for items not included in cash flow	-16 067	-11 421
Cash flow from operations	**-11 507**	**97 536**
Investment activities		
Investments in tangible assets	-83 819	-82 768
Cash flow from investment activities	**-83 819**	**-82 768**
Cash flow for the year	**-95 326**	**14 767**
Liquid assets at the beginning of the year	**328 314**	**313 547**
Liquid assets at the end of the year	**232 988**	**328 314**

NOTES	2022	2021

Note 1 *Accounting principles*

The accounting and valuation principles applied are consistent with the provisions of the Swedish Annual Accounts Act and generally accepted accounting principles (for 2017 onwards, bokföringsnämnden allmänna råd och vägledningar, BFNAR 2012:1 K3).

All amounts are in thousands of Swedish kronor (SEK) unless otherwise stated.

Income

Received grants are reported as income in the period when they were claimed or received. Conditional grants are recognised as income when the associated conditions have been met. Income and revenue from operations, which include own-account funds, are reported as income when they were claimed or received. Grants and other income in foreign currencies have been accounted in the amounts estimated to be received, based on individual assessment.

Employee benefits

Ongoing remuneration to employees, either direct employed or provided via host agreements, in the form of salaries, social security, contributions to pension schemes and staff related insurances are accounted as personnel costs. Other remunerations, in cash, like travel subsistences or as benefits in-kind, like clothing, training and health care are also accounted as personnel costs. Overhead cost on host provided personnel is considered as external services accounted as administration cost.

Financial income

Dividends and interest income are accounted when credited the account.

Receivables

Receivables are stated at the amounts estimated to be received, based on individual assessment.

Receivables and payables in foreign currencies

Receivables and payables in foreign currencies are valued at the closing day rate. Where hedging measures have been used, such as forwarding contracts, the agreed exchange rate is applied. Gains and losses relating to operations are accounted for under other financial income and cost.

Bank accounts in foreign currencies

Bank balances in foreign currencies are valued at the closing day rate.

Fixed assets

Tangible fixed assets are stated at their original acquisition values after deduction of depreciation according to plan. Assets are depreciated systematically over their estimated useful lives. The following periods of depreciation are applied: Buildings 5 - 50 years, Radar systems 3 - 30 years and Equipment and tools 1 - 5 years.

Note 2 *Grants received*

The Associates contributed to the operation during the year in accordance with the EISCAT agreement and later additions. The Affiliates contributed according to agreed annual commitments. Income from European Commission (EC) funded projects were also accounted as received grants. The E3DS1 project started 2017-09-01 and the resulting projects costs were covered by the Associates (see Note 13) and other funds. Received project grants from the Associates are first accounted as prefinancing. Project costs are thereafter covered by withdrawals from prefinancing and at that time accounted as income from operations.

	2022	2021
Associates	40 874	33 764
Affiliates	1 585	1 891
Project grants, EC	3 853	3 114
Project grant, E3DS1	111 382	113 562
	157 694	152 331

Accumulated Associate contributions status as of 2022-12-31

Annual contributions included and for 2022, Finland, Japan (in cash and in-kind), Norway and Sweden were credited for providing E3DS1 project-related funds. These sums are used for EISCATs ownership and time-share calculation

Associate P. R. of China	57 710	53 337
Associate Finland	173 587	146 056
Associate Japan	126 684	117 118
Associate Norway	416 481	330 028
Associate Sweden	317 597	295 373
Associate UK	320 465	317 806
Previous Associates	382 168	382 168
	1 794 691	1 641 886

Note 3 *Revenue from operations*

The Association can, at rates related to the costs involved and as available, sell observation hours to Associates, Affiliates and other parties. Income from such selling of time are considered to be revenue. In 2022, no time-buyers used the systems.

Income from time-buyers	0	0

Note 4 *Other income from operations*

The Association supports visiting users by offering site accommodation and equipment hosting for either campaign brought instruments or for longer deployments. Educational support is done by providing teachers and/or other resources (like laboratory support).

Accommodation	33	4
Instrument hosting agreements	21	21
Educational support	23	18
Other income	7	416
	83	460

Note 5 *Operations*

The annual operating target for all systems together is about 2 500 active (high power mode) hours. For 2022, the budget assumed 2 524 hours and the outcome became 1 966 hours. Passive hours come in addition. Such hours have a minimal effect on cost since the systems do not draw more electricity than in an off mode. Accounted hours are usually lower than the sum of operating hours since some systems have a charge rate that is less than 1-to-1.

Active hours (high-power), per system	*Hours*	*Hours*
EISCAT Svalbard Radar	637	745
UHF system	896	774
VHF system	384	330
Heating system	49	55
	1 966	1 903
Passive hours (receive only)		
Kiruna receiver system	132	117
Sodankylä receiver system	132	117
	264	233

	2022	2021
Accounted hours	*Hours*	*Hours*
Common programmes	768	751
Special programmes	1 046	1 078
Other hours	194	110
	2 007	1 938
Distribution of special programme hours between Associates		
Associate P. R. of China	59	0
Associate Finland	153	165
Associate Japan	123	115
Associate Norway	254	240
Associate Sweden	208	240
Associate UK	153	218
All Associates, AA-runs	96	100
	1 046	1 078
Distribution, other hours		
Affiliates	140	24
EISCAT staff and tests	0	0
Peer-reviewed and TNA campaigns	54	86
Timebuyers	0	0
	194	110

Note 6 *Personnel costs and average number of employees*

The Association employs directly Headquarters and most project staff, currently about 19 positions, including the Director and Director Designate. The Headquarters is located in Kiruna, Sweden. The personnel working at the Kiruna (Sweden), Sodankylä (Finland), Svalbard and Tromsø (Norway) sites are normally not employed by the Association. Instead, the personnel are provided via site contracts by the Swedish Institute of Space Physics (Kiruna site staff but currently none), Oulu University (Sodankylä staff) and the Arctic University of Norway (Tromsø and Svalbard staff). The Association refunds all expenses related to the provided staff, as well as an additional overhead.

Personnel costs in total		
Salaries and emoluments paid to the Director	2 418	2 153
Other personnel, employed and provided via site contracts	17 553	16 539
Social security contributions amounted to	9 064	7 863
of which for pension costs	*4 318*	*3 748*
Other personnel costs	546	115

The current Director is Dr. Axel Steuwer. He joined the Association as Director Designate 2022-05-01 and assumed the role as Director 2023-01-01. His employment is for initially five years. The previous Director, Dr. Craig Heinselman, left the Association 2022-12-31.

Of the pension costs, 373 kSEK (373 kSEK) relates to the previous Director. The Director and all other directly employed staff are included in ITP like occupational pension plans. For the personnel provided via site contracts, the pension plans are handled by their respective employer.

The members of the board (EISCAT Council) and members of committees, who represents Associates and Affiliates, do not receive remunerations from the Association. Travel expenses in connection with Council and committee meetings are normally covered by the Associates and Affiliates. The Association reimburses though the travel costs for Committee Chairpersons and external members.

	2022	2021
Salaries and emoluments and average number of staff per country		
Finland		
Salaries and emoluments	718	686
Average number of staff - men and women	1 + 0	1 + 0
Norway (including Svalbard)		
Salaries and emoluments	4 612	4 725
Average number of staff - men and women	7 + 0	7 + 0
Sweden		
Salaries and emoluments	14 641	13 281
Average number of staff - men and women	15 + 4	14 + 3

Members of the board and Directors at year-end - men and women

The board consist of delegations from every Associate country each having a Delegate (formal member) and up to two Representatives.

Board members (EISCAT Council)	11 + 3	11 + 3
Directors	1 + 0	1 + 0

Note 7 *Changes in designated funds*

Positive numbers - use of designated funds. Negative - transfer to the designated reserves or funds for later use.

Net profit/loss for the year	98 718	107 113
Transfers between regular EISCAT and EISCAT_3D construction project	-16 067	-11 420
Changes to capital operating reserve	-100	-97
Changes to decommissioning fund	-2 651	-2 623
Changes to E3D construction reserve	-3 397	-3 360
Changes to five-year operating reserve	0	-15 500
Changes to funds invested	-75 099	-74 091
Changes to spare parts reserve	-15	4
Changes to surplus fund	-887	0
	501	25

Note 8 *Tangible fixed assets*

Changes in tangible fixed assets.

Buildings		
Opening acquisition value	115 783	96 400
Acquisitions during the year	11 353	19 383
Disposals during the year	0	0
Closing acquisition value	127 135	115 783
Opening accumulated depreciation	-41 668	-41 177
Depreciations during the year	-491	-492
Disposals during the year	0	0
Closing accumulated depreciation	-42 160	-41 668
Closing residual value	84 976	74 115
Radar systems		
Opening acquisition value	476 572	414 152
Acquisitions during the year	71 039	62 420
Disposals during the year	0	0
Closing acquisition value	547 611	476 572
Opening accumulated depreciation	-271 830	-264 616
Depreciations during the year	-7 231	-7 213
Disposals during the year	0	0
Closing accumulated depreciation	-279 061	-271 830
Closing residual value	268 551	204 742

	2022	2021
Equipment and tools		
Opening acquisition value	36 557	36 306
Acquisitions during the year	1 427	965
Disposals during the year	-559	-715
Closing acquisition value	37 424	36 557
Opening accumulated depreciation	-34 448	-34 191
Depreciations during the year	-997	-972
Disposals during the year	559	715
Closing accumulated depreciation	-34 886	-34 448
Closing residual value	2 538	2 109
Sum tangible fixed assets	356 065	280 966

Note 9 *Prepayments and accrued income*

Resources in staff and direct costs spent in ongoing externally funded projects are covered by accrued income until settled by submission of periodic report claims. In 2022, five externally funded projects are ongoing whereof three are EC funded: EGI-ACE, ENVRI-FAIR and PITHIA-NRF.

Prepaid rents	9	9
Prepaid insurances	1 107	852
Accrued income, EGI-ACE project	245	459
Accrued income, ENVRI-FAIR project	1 488	0
Accrued income, PITHIA-NRF project	342	1 459
Accrued income, other projects	24	10
Other items	1 220	219
	4 434	3 008

Note 10 *Bank balances status*

Nordea	232 988	328 314
Cash in hand	0	0
	232 988	328 314

Note 11 *Funds invested status*

Buildings	84 976	74 115
Radar Systems	268 551	204 742
Equipment and Tools	2 538	2 109
	356 065	280 966

Note 12 *Designated funds*

The designated funds are divided into funds and reserves. The Surplus fund and Five-year operating reserve are used for budget transfers between periods in the five years plan. The other funds are earmarked for specific purposes.

Capital operating reserve	3 254	3 154
E3D construction reserve	15 183	11 786
Decommissioning fund	11 850	9 198
Equipment repair fund	754	754
Five-year operating reserve	15 500	15 500
Investment fund	7 753	7 753
Restructuring reserve	4 101	4 101
Spare parts reserve	95	80
Surplus fund	17 962	17 050
	76 452	69 376

Note 13 *EISCAT_3D build grants received but not used*

The construction project, E3DS1, started 2017-09-01 and the completion of the first phase, Stage 1, is delayed. We estimate that most of the installations can be completed in 2023 but system commissioning will continue into 2024.

	2022	2021

Most Associates have now committed to its realisation. An E3DS1 specific funding payment was received from Japan in 2022 and a budgeted transfer from the regular budget to the construction project was done. Associate funds are kept as prefinancing until used in the project. Funds spent are deducted from the different funding sources in accordance with the agreed funding plan.

Changes in EISCAT_3D build grants received but not used

Associate Finland		
Opening balance	62 567	42 948
Received during the year	0	25 749
Used during the year	-19 557	-6 131
Closing balance	43 009	62 567
Associate Japan		
Opening balance	16 367	23 765
Received during the year	1 108	6 898
Used during the year	-7 261	-14 297
Closing balance	10 214	16 367
Associate Norway		
Opening balance	110 432	176 580
Received during the year	0	0
Used during the year	-73 679	-66 148
Closing balance	36 753	110 432
Associate Sweden		
Opening balance	10 884	37 870
Received during the year	0	0
Used during the year	-10 884	-26 986
Closing balance	0	10 884
Regular EISCAT		
Opening balance	0	0
Received during the year	16 263	0
Used during the year	0	0
Closing balance	16 263	0
E3DS1 project finances, gains/losses		
Opening balance	9 560	-1 861
Changes during the year	-196	11 420
Closing balance	9 364	9 560
Local taxes Sweden contribution		
Opening balance	22 073	0
Received during the year	0	26 000
Used during the year	-12 281	-3 927
Closing balance	9 792	22 073
Sum EISCAT_3D received build grants	125 395	231 882

Note 14 *External project grants received but not used*

Most externally funded projects work with prefinancing. For European Commission projects, these are in EUR's. The prefinancing is used to cover reported and approved costs.

EGI-ACE H2020 prefinancing	-42	480
ENVRI-FAIR H2020 prefinancing	1 169	2 725
PITHIA-NRF H2020 prefinancing	3 289	3 019
	4 416	6 224

Annual Report 2021–2022 of the EISCAT Scientific Association

EISCAT Headquarters
Box 812, SE-981 28 Kiruna, Sweden

Scientific contributions: EISCAT Associates and staff

The EISCAT Associates and Affiliates

December 2022

CRIRP

China Research Institute of Radiowave Propagation
China
www.crirp.ac.cn

NFR

Forskningsrådet
Norway
www.forskningsradet.no

NIPR

National Institute of Polar Research
Japan
www.nipr.ac.jp

SA

Suomen Akatemia
Finland
www.aka.fi

UKRI

UK Research and Innovation
United Kingdom
www.ukri.org

VR

Vetenskapsrådet
Sweden
www.vr.se

DLR-SO
Institut für Solar-Terrestrische Physik, Germany
www.dlr.de/so

JHUAPL
Johns Hopkins University Applied Physics Laboratory, United States
www.jhuapl.edu

KASI
Korea Astronomy and Space Science Institute, South Korea
www.kasi.re.kr

KOPRI
Korea Polar Research Institute, South Korea
www.kopri.re.kr

METI
METI International, United States
meti.org

RIAN
Institute of Radio Astronomy, Ukraine
rian.kharkov.ua

EISCAT Scientific Association

Headquarters

EISCAT Scientific Association
Bengt Hultqvists väg 1
SE-981 92 Kiruna
Sweden
Phone: +46 980 79150
www.eiscat.se

Sites

Kiruna

EISCAT Kiruna Site
EISCAT Mottagarstation
SE-981 92 Kiruna
Sweden

Longyearbyen

EISCAT Svalbard Radar
Breinosa, Gruve7-veien
N-9171 Longyearbyen
Norway

Sodankylä

EISCAT Sodankylä Site
Tähteläntie 54B
FIN-996 00 Sodankylä
Finland

Tromsø

EISCAT Tromsø Site
Ramfjordmoen
N-9027 Ramfjordbotn
Norway